AGU PUBLICATIONS

JGR

Journal of Geophysical Research: Earth Surface

RESEARCH ARTICLE

10.1002/2016JF003971

**Key Points:**
- Remotely sensed data capture the spatiotemporal surface velocity response of an ice stream and ice shelf to forcing by ocean tides
- Velocities are modulated nearly 100 km upstream of the grounding zone at the spring-neap tidal period
- Periodic grounding of the ice shelf causes local stress changes that can propagate far upstream due to weakened lateral shear margins

**Supporting Information:**
- Supporting Information S1
- Movie S1
- Movie S2

**Correspondence to:**
B. M. Minchew,
bremin15@bas.ac.uk

**Citation:**
Minchew, B. M., M. Simons, B. Riel, and P. Milillo (2017), Tidally induced variations in vertical and horizontal motion on Rutford Ice Stream, West Antarctica, inferred from remotely sensed observations, *J. Geophys. Res. Earth Surf.*, *122*, 167–190, doi:10.1002/2016JF003971.

Received 27 MAY 2016
Accepted 18 NOV 2016
Accepted article online 22 NOV 2016
Published online 13 JAN 2017



# Tidally induced variations in vertical and horizontal motion on Rutford Ice Stream, West Antarctica, inferred from remotely sensed observations

**B. M. Minchew[1,2], M. Simons[1], B. Riel[1], and P. Milillo[3,4]**

[1]Seismological Laboratory, Division of Geological and Planetary Sciences, California Institute of Technology, Pasadena, California, USA, [2]Now at British Antarctic Survey, Cambridge, UK, [3]School of Engineering, University of Basilicata, Potenza, Italy, [4]Now at Jet Propulsion Laboratory, California Institute of Technology, Pasadena, California, USA

**Abstract** To better understand the influence of stress changes over floating ice shelves on grounded ice streams, we develop a Bayesian method for inferring time-dependent 3-D surface velocity fields from synthetic aperture radar (SAR) and optical remote sensing data. Our specific goal is to observe ocean tide-induced variability in vertical ice shelf position and horizontal ice stream flow. Thus, we consider the special case where observed surface displacement at a given location can be defined by a 3-D secular velocity vector, a family of 3-D sinusoidal functions, and a correction to the digital elevation model used to process the SAR data. Using nearly 9 months of SAR data collected from multiple satellite viewing geometries with the COSMO-SkyMed 4-satellite constellation, we infer the spatiotemporal response of Rutford Ice Stream, West Antarctica, to ocean tidal forcing. Consistent with expected tidal uplift, inferred vertical motion over the ice shelf is dominated by semidiurnal and diurnal tidal constituents. Horizontal ice flow variability, on the other hand, occurs primarily at the fortnightly spring-neap tidal period ($M_{sf}$). We propose that periodic grounding of the ice shelf is the primary mechanism for translating vertical tidal motion into horizontal flow variability, causing ice flow to accelerate first and most strongly over the ice shelf. Flow variations then propagate through the grounded ice stream at a mean rate of ~29 km/d and decay quasi-linearly with distance over ~85 km upstream of the grounding zone.

## 1. Introduction

Ice shelves (the floating extensions of ice sheets) provide resistive back stresses to the seaward flow of glaciers and ice streams [e.g., *Joughin et al.*, 2012a; *Alley et al.*, 2015] that change with variations in ocean temperature, local sea level, and tidal uplift [e.g., *Pritchard et al.*, 2009, 2012; *Joughin et al.*, 2012a; *Makinson et al.*, 2012; *Rignot et al.*, 2014]. These stress changes propagate upstream over a variety of timescales, influencing glacier flow to at least tens of kilometers inland and accounting for some of the recent increases in mass loss from Antarctica [e.g., *Thomas et al.*, 2004; *Scambos et al.*, 2004; *Rignot et al.*, 2004; *Mouginot et al.*, 2014; *Helm et al.*, 2014; *Paolo et al.*, 2015]. The potential for ice shelves to stabilize otherwise unstable ice sheet configurations [*Thomas*, 1979; *Gudmundsson et al.*, 2012; *Gudmundsson*, 2013] and the possibility of catastrophic loss of ice shelves makes stress propagation from floating to grounded ice important for understanding ice sheet evolution over human to geological timescales [e.g., *Scambos et al.*, 2004; *Rignot et al.*, 2004; *Schoof*, 2007; *Joughin et al.*, 2014; *Pollard et al.*, 2015; *DeConto and Pollard*, 2016]. Here we focus on the underlying mechanisms and impact of stress changes driven by ocean tidal uplift on the flow of Rutford Ice Stream (RIS), West Antarctica.

With a strong, well-documented, tidal-timescale flow variability [e.g., *Gudmundsson*, 2006; *Murray et al.*, 2007; *Aðalgeirsdóttir et al.*, 2008; *Gudmundsson*, 2011] and current lack of significant proximal ice shelf thinning [e.g., *Paolo et al.*, 2015] and nonperiodic acceleration [*Scheuchl et al.*, 2012], RIS is a natural laboratory for studying the mechanics of coupled ice shelf-stream systems through dense observations of tidally induced changes in ice flow. RIS is situated immediately east of the Ellsworth Mountain Range and is a major ice stream of the West Antarctic Ice Sheet. RIS flows roughly north-to-south at approximately 1 m/d [*Rignot et al.*, 2011a] into the California-sized Filchner-Ronne Ice Shelf (FRIS; Figure 1), a cold-cavity ice shelf that floats on seawater that is at or near the in situ freezing temperature at the ice-ocean interface [*Nicholls et al.*, 2009]. Recent studies suggest that when averaged over space and time, FRIS is gaining almost as much mass from accumulation as it is losing from melt [*Pritchard et al.*, 2012; *Rignot et al.*, 2013; *Helm et al.*, 2014; *Paolo et al.*, 2015], meaning that

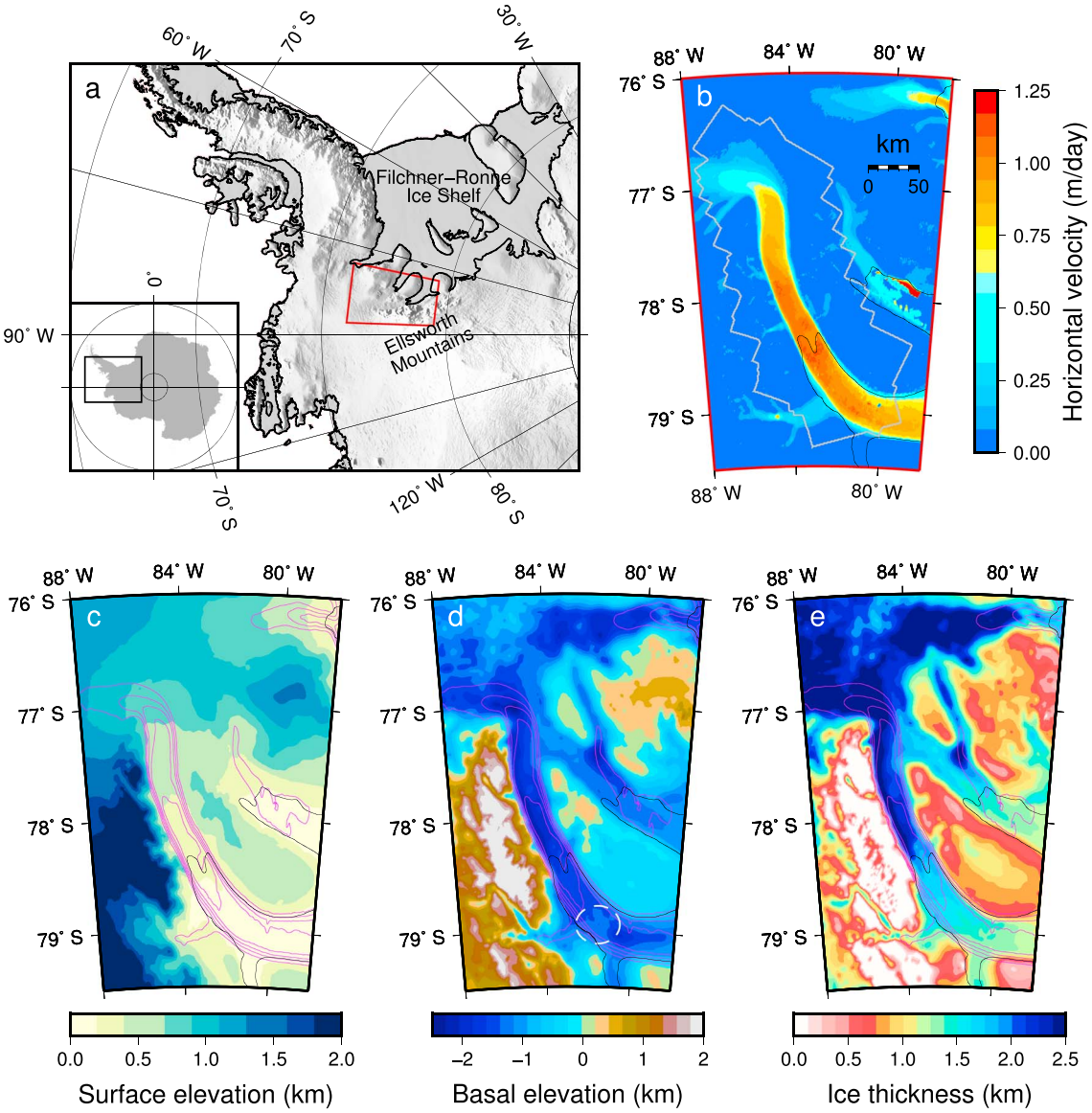


**Figure 1.** (a) Shaded relief map of RIS and surrounding area. Red box indicates the region shown in Figures 1b–1e. (b) Horizontal speed from *Rignot et al.* [2011a]. Gray outline indicates the extent of the CSK observations used in this study. (c and d) Surface and basal elevation in kilometer relative to mean sea level, respectively. (e) Ice thickness in kilometer. Magenta contour lines in Figures 1c–1e indicate smoothed horizontal surface velocity from Figure 1b in 0.2 m/d increments. In all panels, irregular black lines indicate grounding zones. All geometric and grounding line data are from Bedmap2 [*Fretwell et al.*, 2013].

the influence of FRIS on the flow of RIS is approximately constant over multiannual timescales. RIS is about 200 km long and 30 km wide with a typical ice thickness of order 2 km over its grounded portion. The bed of RIS lies more than 1.5 km below sea level and features several prominent topographic highs, areas of deforming subglacial till, active drumlin formation, and an evolving basal hydrological system [*Smith et al.*, 2007; *King et al.*, 2009; *Smith and Murray*, 2009; *Fretwell et al.*, 2013; *Smith et al.*, 2015]. A high in the basal topography is responsible for the sinuosity of the grounding line [*Rignot et al.*, 2011b; *King et al.*, 2016], and there are known ephemeral pinning points beneath the ice shelf [*Goldstein et al.*, 1993; *Rignot*, 1998a; *Schmeltz et al.*, 2001]. Combined tidal amplitudes downstream of the RIS grounding zone can exceed 3 m (Figures 2 and 3), where the largest tidal constituents are the lunar semidiurnal ($M_2$; 12.4 h period) and solar semidiurnal ($S_2$; 12 h period) tides [*Han et al.*, 2005; *Padman et al.*, 2008]. These large tidal amplitudes help give rise to the observed ~20% modulation in ice flow over the spring-neap (14.77 day) tidal cycle [*Gudmundsson*, 2006; *Murray et al.*, 2007]. Building on previous studies of Rutford and its tidally induced ice-flow modulation [*Goldstein et al.*, 1993; *Gudmundsson*, 2011; *Thompson et al.*, 2014; *Rosier et al.*, 2014, 2015], we designed a unique spatially and

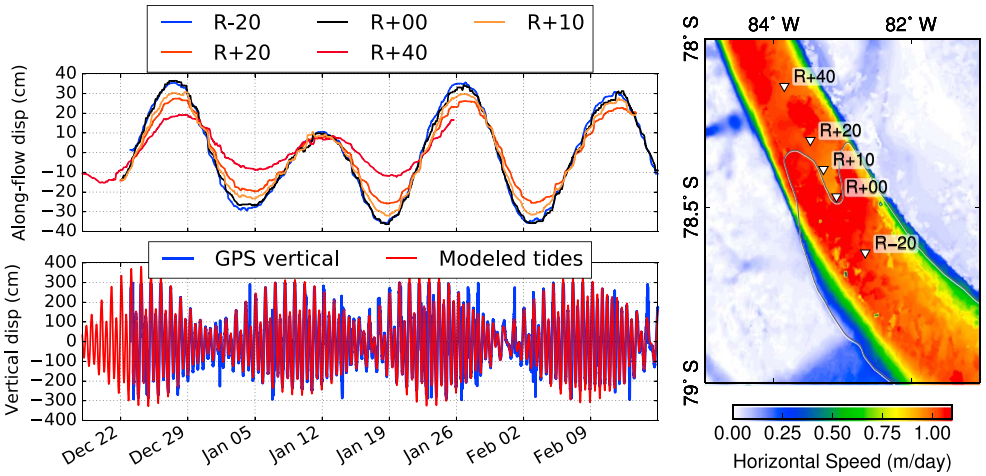


**Figure 2.** Tidally induced flow variation on RIS beginning December 2003. (top left) Along-flow displacements measured with GPS stations. Locations of stations are indicated in the map on the right. Numbers in the GPS designations indicate approximate distance upstream of the grounding line (e.g., R-20 is ≈20 downstream of grounding line and R + 20 is ≈20 upstreams). (bottom left) Vertical motion at R-20 in blue overlain by modeled tidal displacement calculated using CATS2008a_opt [*Padman et al.*, 2002; *Padman and Fricker*, 2005]. GPS data are from *Gudmundsson* [2006, 2011] and are low-pass filtered over a 24 h window. (right) Horizontal speed in m/d from *Rignot et al.* [2011a].

temporally dense synthetic aperture radar (SAR) acquisition campaign that covers the grounded extent of RIS and the landward ~100 km of the ice shelf.

When collected at sufficiently high sampling rates, SAR data are capable of capturing spatiotemporal flow variability [e.g., *Hetland et al.*, 2012], notably in three spatial dimensions with sufficient sampling in several unique viewing geometries [e.g., *Joughin et al.*, 1998; *Joughin*, 2002; *Reeh et al.*, 2003; *Gourmelen et al.*, 2011; *Minchew et al.*, 2016]. Capturing flow variability is possible because a pair of SAR scenes collected from approximately the same spatial position, but at different times, can be used to calculate ice motion along a path parallel to the satellite orbit (azimuth) direction and along the radar line of sight (LOS). Radar LOS vectors are oblique to vertical, meaning they are sensitive to horizontal and vertical displacement, and are often orthogonal to the instrument velocity vector. In both azimuth and LOS cases, measurements of displacement are attainable using several approaches, including interferometric (InSAR) and 2-D cross-correlation methods [e.g., *Rosen et al.*, 2000; *Joughin*, 2002; *Bamler and Eineder*, 2005; *Simons and Rosen*, 2015]. InSAR is the most precise method and generally offers higher spatial resolution [*Rosen et al.*, 2000; *Simons and Rosen*, 2015], while cross-correlation methods, such as feature or speckle tracking, are more robust to large displacements,

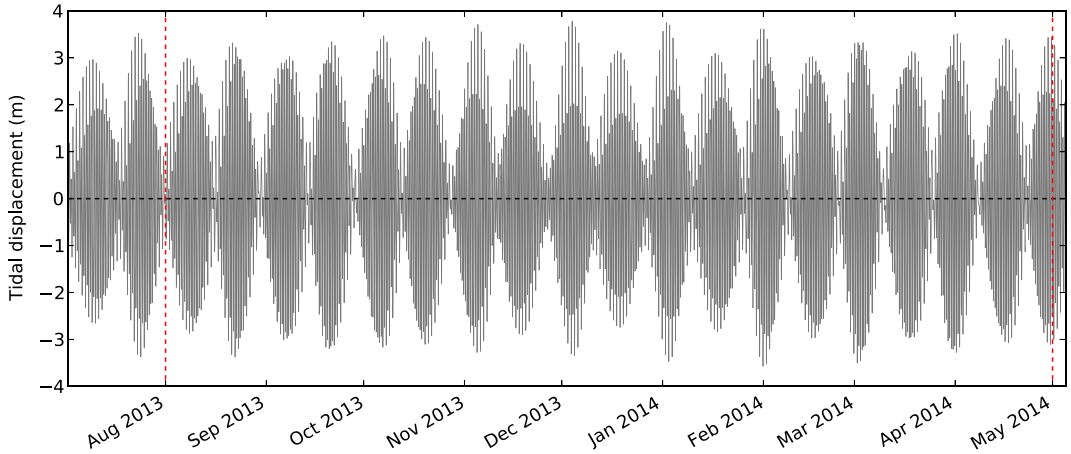


**Figure 3.** Modeled tidal displacement at location R-20 for the CSK observational period calculated using CATS2008a_opt [*Padman et al.*, 2002; *Padman and Fricker*, 2005]. Vertical red dashed lines indicate the approximate start and stop time of the CSK data collection.

minor changes in target scattering properties, and in certain terrain types where InSAR methods yield low signal-to-noise ratios [*Gray et al.*, 2001; *Joughin*, 2002]. Though not considered further in this study, measurements of displacement can also be gleaned from optically sensed data along two horizontal dimensions [e.g., *Scambos et al.*, 1992].

Here we develop a Bayesian method for inferring time-dependent, 3-D surface velocity fields (i.e., 4-D velocity fields) from a time series of displacement fields calculated using SAR and optical remote sensing observations collected from multiple viewing geometries. Our method for inferring 4-D velocity fields is independent of the approach used to calculate displacements and relies only on having three or more unique observation vectors and an appropriate time sampling given the desired functional form of the posterior model. In developing the method, we assume that the data are appropriately sampled in three spatial dimensions and have sufficient sampling rates and durations to constrain the specified temporal basis functions. We demonstrate and validate our method on a synthetic ice stream designed to resemble RIS, including all known temporal variabilities in vertical and horizontal ice flow, before presenting results from SAR data collected over RIS.

## 2. Methodology

### 2.1. Time-Dependent Displacement

In the most general case, observed displacements can be described as a sum of a secular velocity and numerous periodic and transient terms [e.g., *Hetland et al.*, 2012]. Here we are primarily interested in the influence of ocean tides on ice stream flow, so we consider the special case where the instantaneous 3-D displacement vector $\mathbf{u}$ of a point on the surface at time $t$ and location $\mathbf{r}$ (relative to the observer) is a function of a 3-D secular velocity vector $\mathbf{v}'(\mathbf{r})$ and a family of 3-D sinusoidal functions such that

$$\mathbf{u}(\mathbf{r},t) = \mathbf{v}'t + \sum_{i=1}^{k} \begin{bmatrix} a_i^{\hat{e}} \sin\left(\omega_i t + \phi_i^{\hat{e}}\right) \\ a_i^{\hat{n}} \sin\left(\omega_i t + \phi_i^{\hat{n}}\right) \\ a_i^{\hat{u}} \sin\left(\omega_i t + \phi_i^{\hat{u}}\right) \end{bmatrix}. \tag{1}$$

Each sinusoid $i$ has angular frequency $\omega_i$, amplitude $a_i^{\hat{\xi}} = a_i^{\hat{\xi}}(\mathbf{r})$, and phase $\phi_i^{\hat{\xi}} = \phi_i^{\hat{\xi}}(\mathbf{r})$ for $\hat{\xi} = \hat{e}, \hat{n}, \hat{u}$, representing three mutually orthogonal coordinate directions, hereafter taken to be east, north, and up, respectively. Note that in equation (1) we assume that all data are referenced to areas with zero displacement but that this assumption is not a strict requirement because equation (1) could be expanded to facilitate simultaneous inferences of a planar offset for each displacement field.

Using pairs of SAR (or optical) images, we measure the displacement of a target over a given time interval. These measurements contain noise, which we separate according to errors in LOS displacements arising from nonzero spatial separation between the SAR antenna during each image acquisition—commonly referred to as the perpendicular or interferometric baseline—and noise caused by decorrelation, instrument radiation, tropospheric delay, and other noise sources [*Rosen et al.*, 2000; *Simons and Rosen*, 2015]. The measured displacement of the target relative to the observer over the time interval $[t_a, t_b]$ along observational unit vector $\hat{\boldsymbol{\ell}}$ is then

$$d_{ab}(\hat{\boldsymbol{\ell}}, \mathbf{r}, t_a, t_b) = \hat{\boldsymbol{\ell}} \cdot \left(\mathbf{u}_a - \mathbf{u}_b\right) + b_{ab} + \epsilon_{ab} \tag{2}$$

where $b_{ab}$ represents error arising from nonzero baseline, $\epsilon_{ab}$ accounts for all other noise factors, and $\mathbf{u}_\xi = \mathbf{u}(\mathbf{r}, t_\xi)$ for $\xi = a, b$. Later we employ linear matrix-based inverse methods to infer the velocity field, so we apply a basic trigonometric identity and write the displacement over the given time interval as follows:

$$\mathbf{u}_a - \mathbf{u}_b = \mathbf{v}'\Delta t_{ab} + \sum_{i=1}^{k} \left[\mathbf{c}_i \Delta p_{i_{ab}}^{\cos} + \mathbf{s}_i \Delta p_{i_{ab}}^{\sin}\right] \tag{3}$$

where

$$\Delta t_{ab} = t_b - t_a \tag{4}$$

$$\Delta p_{i_{ab}}^{\cos} = \cos\left(\omega_i t_b\right) - \cos\left(\omega_i t_a\right) \tag{5}$$

$$\Delta p_{i_{ab}}^{\sin} = \sin\left(\omega_i t_b\right) - \sin\left(\omega_i t_a\right) \tag{6}$$

$$\mathbf{c}_i = \left[\, a_i^{\hat{e}} \sin\left(\phi_i^{\hat{e}}\right) \;\; a_i^{\hat{n}} \sin\left(\phi_i^{\hat{n}}\right) \;\; a_i^{\hat{u}} \sin\left(\phi_i^{\hat{u}}\right) \,\right]^T \tag{7}$$

$$\mathbf{s}_i = \left[\, a_i^{\hat{e}} \cos\left(\phi_i^{\hat{e}}\right) \;\; a_i^{\hat{n}} \cos\left(\phi_i^{\hat{n}}\right) \;\; a_i^{\hat{u}} \cos\left(\phi_i^{\hat{u}}\right) \,\right]^T . \tag{8}$$

After inferring the components of $\mathbf{c}_i$ and $\mathbf{s}_i$, amplitude and phase for each sinusoid can be recovered using the identities:

$$a_i^{\hat{\varsigma}} = \sqrt{\left(c_i^{\hat{\varsigma}}\right)^2 + \left(s_i^{\hat{\varsigma}}\right)^2} \tag{9}$$

$$\phi_i^{\hat{\varsigma}} = \tan^{-1}\left(c_i^{\hat{\varsigma}} / s_i^{\hat{\varsigma}}\right). \tag{10}$$

When displacement data are collected with a SAR instrument, it may be possible to glean additional information about the local (time-invariant) topography. This capability arises from the fact that observations collected along the oblique radar LOS are sensitive to topography whenever the perpendicular baseline is nonzero [e.g., *Rosen et al.*, 2000]. The topographic contribution to the signal is commonly accounted for during processing using an independently derived digital elevation model (DEM). When the DEM is known but is expected to have errors or is lower resolution than the SAR data, the observed displacement signal will contain topographic residuals, $\delta z_d$. These residuals contribute to the SAR measurements as follows:

$$b_{ab} = \psi_{ab} \delta z_d \tag{11}$$

$$\psi_{ab} = \begin{cases} B_{\perp_{ab}} / (r_0 \sin\theta_0) & \text{along LOS} \\ 0 & \text{otherwise} \end{cases} \tag{12}$$

where $B_{\perp_{ab}}$ is the perpendicular baseline and $r_0$ and $\theta_0$ are the range and incidence angle (measured relative to local up) to a smooth reference surface, respectively [*Rosen et al.*, 2000; *Simons and Rosen*, 2015]. Caution should be exercised when interpreting inferred $\delta z_d$ values because they may contain significant errors caused by inaccurate estimates of $B_{\perp_{ab}}$, noise in the displacement measurements, and other factors (see Appendix A).

### 2.2. Displacement Model

To infer solutions at each grid point in the velocity field, we cast the problem in a general matrix form:

$$\mathbf{Gm} = \mathbf{d} \tag{13}$$

where $\mathbf{d}$ is the vector of observed displacements, $\mathbf{m}$ is the model vector, and $\mathbf{G}$ is the design matrix. For any given grid location, the model vector has the form

$$\mathbf{m} = \left[\, \mathbf{v}' \;\; \mathbf{c}_1 \;\; \mathbf{s}_1 \;\; \cdots \;\; \mathbf{c}_k \;\; \mathbf{s}_k \;\; \delta z_d \,\right]^T \tag{14}$$

for $k$ periodic functions, and a corresponding design matrix for $q$ pairs given as follows:

$$\mathbf{G} = \begin{bmatrix} \hat{\boldsymbol{\ell}}_1 \Delta t_1 & \hat{\boldsymbol{\ell}}_1 \Delta p_{1_1}^{\cos} & \hat{\boldsymbol{\ell}}_1 \Delta p_{1_1}^{\sin} & \cdots & \hat{\boldsymbol{\ell}}_1 \Delta p_{k_1}^{\cos} & \hat{\boldsymbol{\ell}}_1 \Delta p_{k_1}^{\sin} & \psi_1 \\ \vdots & & & \ddots & & & \vdots \\ \hat{\boldsymbol{\ell}}_q \Delta t_q & \hat{\boldsymbol{\ell}}_q \Delta p_{1_q}^{\cos} & \hat{\boldsymbol{\ell}}_q \Delta p_{1_q}^{\sin} & \cdots & \hat{\boldsymbol{\ell}}_q \Delta p_{k_q}^{\cos} & \hat{\boldsymbol{\ell}}_q \Delta p_{k_q}^{\sin} & \psi_q \end{bmatrix}. \tag{15}$$

Note that we number $ab$ pairs from 1 to $q$ in equation (15) and omit the transpose sign on the interior vectors in equations (14) and (15) for clarity.

Following *Minchew et al.* [2015], who applied Bayesian methods described by *Tarantola* [2005] to the problem of inferring 3-D velocity fields using InSAR data collected from multiple LOS vectors, we can write the posterior model vector $\tilde{\mathbf{m}}$, i.e., the best fit solution to equation (13), in its most general form as follows:

$$\tilde{\mathbf{m}} = \left(\mathbf{G}^T\mathbf{C}_d^{-1}\mathbf{G} + \mathbf{C}_m^{-1}\right)^{-1}\left(\mathbf{G}^T\mathbf{C}_d^{-1}\mathbf{d} + \mathbf{C}_m^{-1}\mathbf{m}_0\right) \tag{16}$$

where $\mathbf{m}_0$ is the prior model vector and $\mathbf{C}_d$ and $\mathbf{C}_m$ are the data and prior model covariance matrices, respectively [*Tarantola*, 2005]. The data covariance matrix, $\mathbf{C}_d$, accounts for errors and interdependencies of the displacement measurements, while the prior model covariance matrix, $\mathbf{C}_m$, accounts for a priori assumptions of model parameters, their interdependencies, and possibly the spatial characteristics of the model. The form of $\mathbf{C}_d$ is based on the characteristics of the data, whereas the form of $\mathbf{C}_m$ should be chosen based on the physical processes under consideration.

### 2.3. Data and Prior Model Covariance Matrices

The data covariance matrix, $\mathbf{C}_d$, accounts for observational imperfections, which in this case are errors and interdependencies of displacement fields. Possible sources of error include atmospheric phase delay in LOS observations [e.g., *Hanssen*, 2001; *Emardson et al.*, 2003; *Lohman and Simons*, 2005], high measurement noise [e.g., *Rodriguez and Martin*, 1992; *Hanssen*, 2001; *Zebker and Villasenor*, 1992], and spatial dependences within the displacement data arising from filtering. In practice, it is often difficult to estimate atmospheric phase delay within the geographic regions of interest in this study. For this reason and for simplicity and computational tractability, we assume that measurement errors are spatially and temporally incoherent, resulting in a diagonal data covariance matrix defined as follows:

$$C_{d_{ij}} = \begin{cases} \sigma_{d_i}^2 & i = j \\ 0 & i \neq j \end{cases} \tag{17}$$

where $\sigma_{d_i}^2$ is the variance of displacement field $i$. For InSAR data, the variance can be estimated from InSAR correlation $\gamma_i$ such that [*Rodriguez and Martin*, 1992]

$$\sigma_{d_i}^2 = \frac{\lambda}{4\pi N_{u_i}}\frac{1-\gamma_i^2}{\gamma_i^2} \tag{18}$$

where $\lambda$ is the radar wavelength and $N_{u_i}$ is the number of pixels in the filtering window applied to displacement field $i$ [e.g., *Rosen et al.*, 2000; *Simons and Rosen*, 2015]. Variances for displacements calculated using feature or speckle tracking can be estimated from the curvature of the correlation surface [*Joughin*, 2002].

There are a number of valid options for the form of $\mathbf{C}_m$. One option is to impose spatial smoothness in the velocity field, an approach that can incur high computational costs because all model parameters within areas of interest must be inferred simultaneously [*Minchew et al.*, 2015]. Our experience with the data presented in this study suggests that spatial smoothing is unnecessary. Instead, we found that there can be trade-offs between the sinusoidal amplitudes and phases when inferring multiple periodic functions. GPS data collected in our study area [e.g., *Murray et al.*, 2007] show that variations in horizontal ice flow occur over fortnightly and longer periods, while vertical motion occurs primarily at semidiurnal and diurnal periods. Therefore, we adopt a form for $\mathbf{C}_m$ that penalizes nonzero amplitudes for sinusoids with periods shorter than a user-defined reference period in the horizontal components and sinusoids with periods longer than a user-defined reference in the vertical components. This form of $\mathbf{C}_m$ is diagonal and defined as follows:

$$\mathbf{C}_m^{-1} = \mathrm{diag}\left[\,0\;\;0\;\;0\;\;\Omega_1^h\;\;\Omega_1^h\;\;\Omega_1^v\;\;\cdots\;\;\Omega_k^h\;\;\Omega_k^h\;\;\Omega_k^v\;\;0\,\right] \tag{19}$$

$$\Omega_i^h = \kappa_p\left(\frac{\omega_i}{\omega_{ref}^h} - 1\right)^2 \tag{20}$$

$$\Omega_i^v = \kappa_p\left(\frac{\omega_{\mathrm{ref}}^v}{\omega_i} - 1\right)^2 \tag{21}$$

where $\kappa_p$ is a scalar weighting parameter (whose units are assigned such that the units of $\mathbf{C}_m^{-1}$ match those of $\mathbf{G}^T\mathbf{C}_d^{-1}\mathbf{G}$) that can be thought of like a regularization parameter commonly used in Tikhonov regularization and $\omega^h_{\text{ref}}$ and $\omega^v_{\text{ref}}$ are the reference angular frequencies for horizontal and vertical periodic functions, respectively. In general, $\omega^h_{\text{ref}}$ and $\omega^v_{\text{ref}}$ should be the frequency with the largest expected amplitude in each spatial dimension. Consequently, nonzero elements of $\mathbf{C}_m^{-1}$ correspond to elements of $\widetilde{\mathbf{m}}$ that we expect to be small. Therefore, it follows that $\mathbf{C}_m^{-1}\mathbf{m}_0 \ll \mathbf{G}^T\mathbf{C}_d^{-1}\mathbf{d}$, reducing equation (16) to

$$\widetilde{\mathbf{m}} = \left(\mathbf{G}^T\mathbf{C}_d^{-1}\mathbf{G} + \mathbf{C}_m^{-1}\right)^{-1}\mathbf{G}^T\mathbf{C}_d^{-1}\mathbf{d}. \tag{22}$$

a form similar to Tikhonov regularized least squares.

### 2.4. Formal Error Estimation

The first term in equation (22) is the posterior model covariance matrix:

$$\widetilde{\mathbf{C}}_m = \left(\mathbf{G}^T\mathbf{C}_d^{-1}\mathbf{G} + \mathbf{C}_m^{-1}\right)^{-1} \tag{23}$$

which provides estimates of the formal errors in $\widetilde{\mathbf{m}}$ [*Tarantola*, 2005]. Elements along the diagonal are the variances for each component of $\widetilde{\mathbf{m}}$, while off-diagonal elements provide the covariances between model parameters. As a result, higher amplitudes in the components of $\widetilde{\mathbf{C}}_m$ indicate higher uncertainty in $\widetilde{\mathbf{m}}$.

Given the form of the design matrix $\mathbf{G}$, phase and amplitude errors are implicit in the posterior model covariance matrix $\widetilde{\mathbf{C}}_m$, while errors for the components of $\mathbf{c}_i$ and $\mathbf{s}_i$ are explicit. To derive errors for amplitude and phase, let us first write the errors for the components of $\mathbf{c}_i$ and $\mathbf{s}_i$ as functions of amplitude and phase errors:

$$\begin{aligned}\sigma^2_{c_i^{\hat{\xi}}} &= \left(\frac{\partial c_i^{\hat{\xi}}}{\partial a_i^{\hat{\xi}}}\right)^2 \sigma^2_{a_i^{\hat{\xi}}} + \left(\frac{\partial c_i^{\hat{\xi}}}{\partial \phi_i^{\hat{\xi}}}\right)^2 \sigma^2_{\phi_i^{\hat{\xi}}} \\ &= \sin^2\left(\phi_i^{\hat{\xi}}\right)\sigma^2_{a_i^{\hat{\xi}}} + \left(a_i^{\hat{\xi}}\cos\left(\phi_i^{\hat{\xi}}\right)\right)^2 \sigma^2_{\phi_i^{\hat{\xi}}}\end{aligned} \tag{24}$$

$$\begin{aligned}\sigma^2_{s_i^{\hat{\xi}}} &= \left(\frac{\partial s_i^{\hat{\xi}}}{\partial a_i^{\hat{\xi}}}\right)^2 \sigma^2_{a_i^{\hat{\xi}}} + \left(\frac{\partial s_i^{\hat{\xi}}}{\partial \phi_i^{\hat{\xi}}}\right)^2 \sigma^2_{\phi_i^{\hat{\xi}}} \\ &= \cos^2\left(\phi_i^{\hat{\xi}}\right)\sigma^2_{a_i^{\hat{\xi}}} + \left(a_i^{\hat{\xi}}\sin\left(\phi_i^{\hat{\xi}}\right)\right)^2 \sigma^2_{\phi_i^{\hat{\xi}}}\end{aligned} \tag{25}$$

for coordinate $\zeta$ and periodic function $i$. Equations (24) and (25) are a system of two equations with two unknowns so long as $a_i^{\hat{\xi}} > 0$ and $\phi_i^{\hat{\xi}} \neq \xi\pi/4$ for $\xi = 1, 3, 5,$ or 7. Solving the system of equations for amplitude and phase errors yields

$$\sigma^2_{a_i^{\hat{\xi}}} = \frac{\sigma^2_{c_i^{\hat{\xi}}}\sin^2\left(\phi_i^{\hat{\xi}}\right) - \sigma^2_{s_i^{\hat{\xi}}}\cos^2\left(\phi_i^{\hat{\xi}}\right)}{\sin^4\left(\phi_i^{\hat{\xi}}\right) - \cos^4\left(\phi_i^{\hat{\xi}}\right)} \tag{26}$$

$$\sigma^2_{\phi_i^{\hat{\xi}}} = \frac{-\sigma^2_{c_i^{\hat{\xi}}}\cos^2\left(\phi_i^{\hat{\xi}}\right) + \sigma^2_{s_i^{\hat{\xi}}}\sin^2\left(\phi_i^{\hat{\xi}}\right)}{\left(a_i^{\hat{\xi}}\right)^2\left(\sin^4\left(\phi_i^{\hat{\xi}}\right) - \cos^4\left(\phi_i^{\hat{\xi}}\right)\right)} \tag{27}$$

indicating that both amplitude and phase errors are functions of the inferred phase value and the respective $c_i^{\hat{\xi}}$ and $s_i^{\hat{\xi}}$ errors. Phase errors also scale as the inverse of amplitude squared, meaning that phase values in areas with small sinusoidal amplitudes are likely to be erroneous. In the extreme case, phase errors approach infinity as amplitude approaches zero, which does not pose a problem for interpreting the data because the phase of an inferred near-zero-amplitude periodic function contains little-to-no information. The other singularity in equations (26) and (27) arises from the fact that equations (24) and (25) are equivalent when phase is an odd-integer multiple of $\pi/4$, leaving one equation and two unknowns. In that case, it is not possible

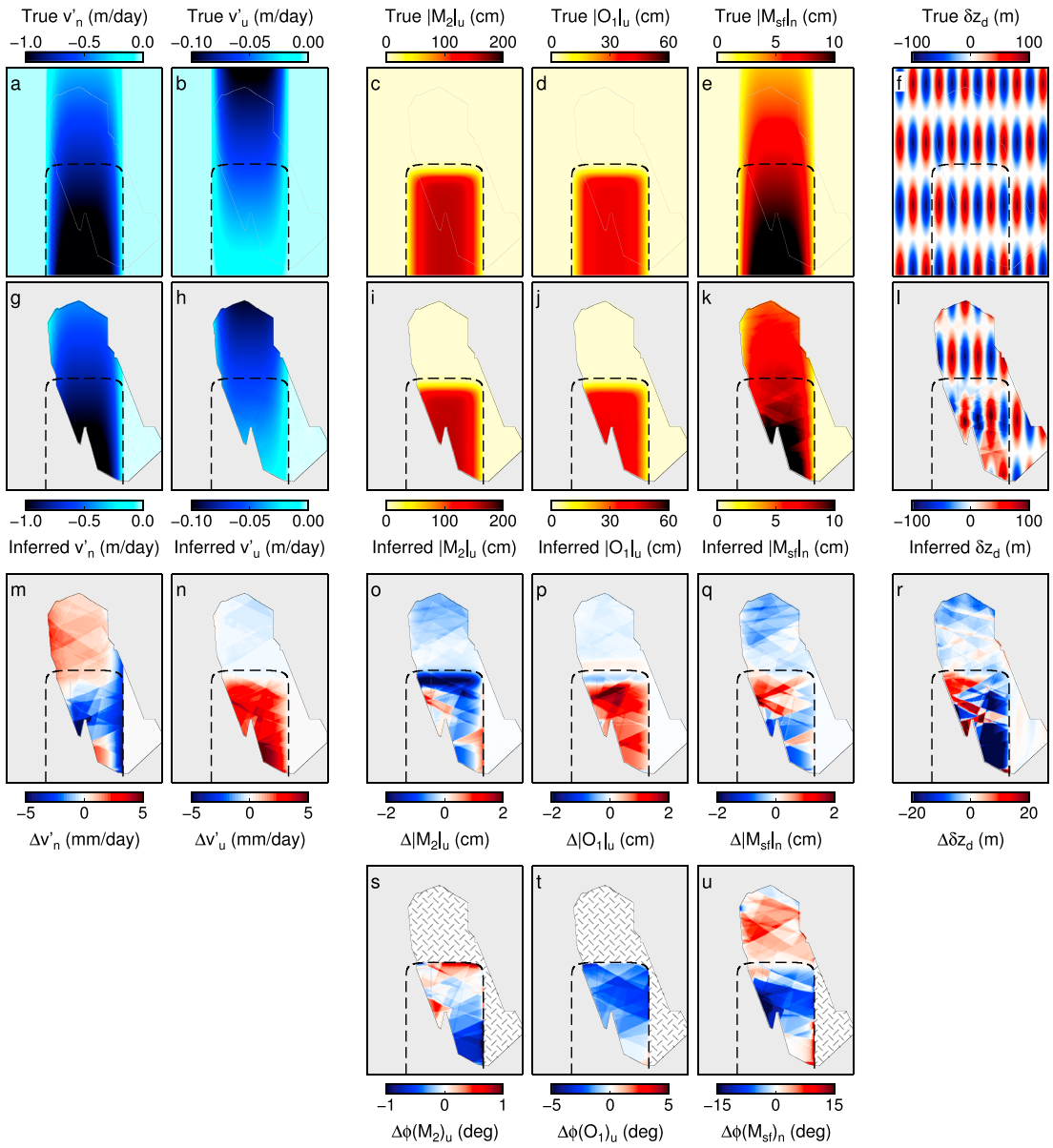


**Figure 4.** True and inferred values for a south flowing synthetic ice stream. (a–f) Salient synthetic (i.e., true) ice stream components, including (a and b) nonzero secular velocity values, (c–e) primary sinusoidal amplitudes, and (f) residual topography. (g–l) Inferred values corresponding to Figures 4a–4f. (m–r) Differences between true and inferred values. (s–u) Misfits between true and inferred phase values. True phase values are spatially constant, and crosshatched regions indicate near-zero amplitudes. Dashed lines in all figures indicate the grounding line.

to uniquely solve for amplitude and phase errors from $\sigma_{c_l^{\hat{\xi}}}$ and $\sigma_{s_l^{\hat{\xi}}}$. This latter singularity is unlikely to pose a problem in practice because measurement noise, the accuracy of efficient numerical solvers, and floating point precision in modern computers diminish the likelihood that phase values will be exact integer multiples of $\pi/4$ over meaningful spatial scales.

While the posterior model covariance matrix provides formal error estimates that account for observational noise and nonideal viewing geometries, it is advantageous in some cases, such as observational planning, to estimate only the contribution of nonideal viewing geometries to uncertainty in the posterior model. A set of ideal viewing geometries has consistent, oblique incidence angles, full azimuthal coverage, and constant azimuthal spacing between platform velocity vectors [*Minchew et al.*, 2015], conditions that are rarely

achievable in practice because of orbital or other constraints. Estimates of uncertainty attributable to nonideal viewing geometries are contained in the noise-sensitivity matrix:

$$\mathbf{S} = \left(\mathbf{G}^T\mathbf{G}\right)^{-1}. \tag{28}$$

The diagonal terms of $\mathbf{S}^{-1}$ are the sums of the squares of the corresponding design matrix column, and the off-diagonal terms are the sums of the cross products of the design matrix components. The off-diagonal components of $\mathbf{S}^{-1}$ indicate coupling between respective posterior model constituents that results from a nonideal set of viewing geometries, while the diagonal components quantify how measurement errors propagate into the components of $\tilde{\mathbf{m}}$. When the viewing geometry is ideal, all off-diagonal components are zero, and each diagonal component in $\mathbf{S}$ is simply the inverse of the respective diagonal component in $\mathbf{G}^T\mathbf{G}$. When the viewing geometry is nonideal, off-diagonal components in $\mathbf{S}^{-1}$ contribute to the diagonal components through the adjugate and determinant of $\mathbf{S}^{-1}$. Differential incidence angles, inconsistent azimuthal spacing, or incomplete azimuthal coverage in the viewing geometries all lead to nonzero off-diagonal components in $\mathbf{S}^{-1}$ and increased sensitivity to measurement noise.

### 2.5. Tests With Synthetic Data

To evaluate the methods developed in the previous sections and explore how well anticipated ice flow on RIS is captured by different families of sinusoidal functions, we developed a synthetic ice stream similar to RIS in both geographic extent and flow characteristics. We compute the secular velocity profile using an idealized ice stream model [*Raymond*, 1996; *Cuffey and Paterson*, 2010], placing grounded ice in the north and an ice shelf in the south with a smooth transition in vertical tidal influence between grounded and floating ice. The modeled horizontal and vertical ice velocity components vary sinusoidally at 11 different periods, each corresponding to a defined tidal constituent. We assigned vertical and horizontal amplitude and phase values for each sinusoid using results from more than 2 years of GPS measurements collected on RIS by *Murray et al.* [2007]. Details of the synthetic ice stream can be found in Text S1 in the supporting information.

We observe the synthetic ice stream using the same observational plan as for the data collected over RIS to ensure consistency between and applicability of the synthetic tests to the data used in this study. For convenience, we truncate the geographic region to the southern 3/4 of the observational domain. Observations of the synthetic ice stream are calculated using equation (2) and result in displacement fields like those attainable from SAR (and optical) data. To each of these synthetic displacement fields we add zero mean Gaussian white noise with 2 cm standard deviations, approximately double the typical noise level in the RIS data discussed herein. Values for $\omega^h_{\text{ref}}$, $\omega^v_{\text{ref}}$, and $\kappa_p$ are equivalent to those used for the RIS data (see section 4).

Based on several tests using different families of sinusoidal terms, we conclude that the posterior model containing only $M_2$ (12.4 h period), $O_1$ (25.8 h period), and $M_{\text{sf}}$ (14.77 day period) tidal periods produces inferred secular velocity and sinusoidal amplitude and phase values that most closely agree with the prescribed synthetic values (Figure 4). We find that all inferred values aside from residual topography, $\delta z_d$, are within 10% of the corresponding synthetic, or true, value in vertical and horizontal dimensions. Secular velocity components have inferred values that are within 1% of true values over grounded ice, a misfit that increases to 5% in the vertical secular velocity over the ice shelf. (Larger errors in horizontal secular velocity within the shear margins are caused by resampling the synthetic displacement fields to a coarser grid.) Vertical amplitudes for $M_2$ and $O_1$ period sinusoids and horizontal amplitudes for the $M_{\text{sf}}$ period sinusoid are fit within 5% of the true values within most areas of interest, as are the corresponding phase values in areas with nonzero amplitudes. Isolated areas with large amplitude and phase misfits arise from nonideal viewing geometries. The only component that is poorly fit in the synthetic tests is residual topography, where the largest misfits are over the ice shelf, as expected (see Appendix A). A more complete discussion of the synthetic results is in the supporting information Text S1.

## 3. Data and Processing Methodology

COSMO-SkyMed (CSK), which is operated by the Italian Space Agency (ASI), collected SAR data over RIS for approximately 9 months beginning in August 2013. The data acquisition plan covers all of the grounded ice and the landward ~100 km of the floating ice shelf from ascending and descending orbits (Figure 1b). All four CSK satellites collected data, each repeating a given orbit track every 16 days. CSK satellite orbits are offset from one another at irregular intervals, yielding SAR pairs with interim times between subsequent SAR

acquisitions of 1, 3, 4, and 8 days. All CSK satellites carry nearly identical X-band (3.1 cm wavelength; 9.6 GHz) SAR systems, and we use the Stripmap-HIMAGE products, which provide raw spatial resolution as fine as 3 m [*CSK*, 2009].

We processed the CSK data (beginning with level 0 raw data) [*CSK*, 2009] using the InSAR Scientific Computing Environment (ISCE), a radar-processing software package developed primarily at NASA's Jet Propulsion Laboratory [*Zebker et al.*, 2010; *Rosen et al.*, 2012]. We developed the top-level software used to calculate the LOS and azimuth offset fields (now included as part of the publicly released version of ISCE) by adopting basic functionality from both ISCE and the Repeat Orbit Interferometry Package (ROI_PAC) [*Rosen et al.*, 2004]. To calculate offset fields, we prescribed the 2-D cross-correlation windows to be $64 \times 64$ pixels, defined in the single-look complex (SLC) image grid, with a step size of 32 SLC-pixels in each direction. Using tools available in ISCE, we accounted for topography in the LOS offsets using the Bedmap2 DEM [*Fretwell et al.*, 2013], resampled to a 25 m grid using bicubic interpolation implemented in Generic Mapping Tools [*Wessel et al.*, 2013], and geocoded all results to the resampled DEM. Following topographic correction and prior to geocoding, we filtered the resulting LOS and azimuth offset fields using a moving-window median filter with an $8 \times 8$ pixel window (where pixel size is now defined by the offset-field grid given in radar, or range-Doppler, coordinates). To account for any small planar trends in the offset fields, we estimated and removed linear or quadratic trends from areas with relatively stagnant ice. This latter step helps ensure greater accuracy and reasonable transitions in the final velocity field at the edges of individual satellite tracks but does not significantly alter any of the inferred offset field values.

Using this processing scheme, we derive 4448 displacement fields along 32 unique tracks with acquisition dates and times that are <10 days apart. Out of the total number of displacement fields, only 1644 have high enough coherence over RIS to be useful for our analysis and examples of these displacement fields are given in Figures S12–S14. The reason we only derive displacement fields with interim times <10 days and that only 36% of the data were coherent over the study area is that much of RIS is covered by dry snow [e.g., *Doake et al.*, 2001] whose surface is relatively flat and featureless at radar wavelengths, particularly in areas with little or no ice flow. Snow is a lossy medium that scatters relatively little energy back to the radar antenna and high-frequency radar systems, such as those aboard CSK, tend to have much of their energy scattered from within a few wavelengths of the surface [e.g., *Ulaby et al.*, 1986]. Owing to snow accumulation and wind, the radar near surface on RIS is ephemeral, diminishing the probability of generating long timescale ($\Delta t > 10$ days) displacement fields. While shorter timescale displacement fields also can be incoherent, the scattering properties of the glacier surface are more likely to remain approximately constant as the time between radar acquisitions is reduced. Therefore, the ability to acquire multiple SAR acquisitions over short timescales is a key advantage to using satellite constellations, such as CSK, to infer spatiotemporal variability in ice flow.

## 4. Results

We report inferences of secular velocity and the $M_2$ (12.4 h period), $O_1$ (25.8 h period), and $M_{sf}$ (14.77 day period) family of sinusoids (see section 2.5 and supporting information Text S1 for the motivation behind and consequences of choosing these tidal constituents) gleaned from 1644 displacement fields calculated using pairs of CSK acquisitions with interim times $<$ 10 days (Figure S15). The final spatial resolution is approximately 100 m in each horizontal dimension. GPS and tidal observations indicate that vertical ice shelf motion occurs primarily at semidiurnal and diurnal periods, while horizontal flow variations occur primarily at the $M_{sf}$ period, so we set $\omega^v_{\text{ref}} = 2\pi/0.52$ rad/d and $\omega^h_{\text{ref}} = 2\pi/14.77$ rad/d (equations (20) and (21)). Based on tests with the synthetic ice stream, we set $\kappa_p = 10$ m$^{-2}$ in the prior model covariance matrix (equation (19)). We exclude estimates of the DEM correction because small perpendicular baselines and relatively large uncertainties associated with displacement fields calculated from 2-D cross-correlation methods cause unacceptable errors in the inferred DEM corrections (Appendix A). Movies showing how the vertical position of the ice shelf (Movie S1) and horizontal ice flow (Movie S2) vary in time are included as part of the supporting information.

### 4.1. Secular Fields

The secular velocity and strain rate fields provide both validation of the inferred time-dependent velocity field and insight into the response of RIS to tidal forcing. We present here the secular fields that are most relevant to understanding the tidal-timescale variations in ice flow. Additional secular fields and associated formal error estimates are given in the supporting information Text S2.

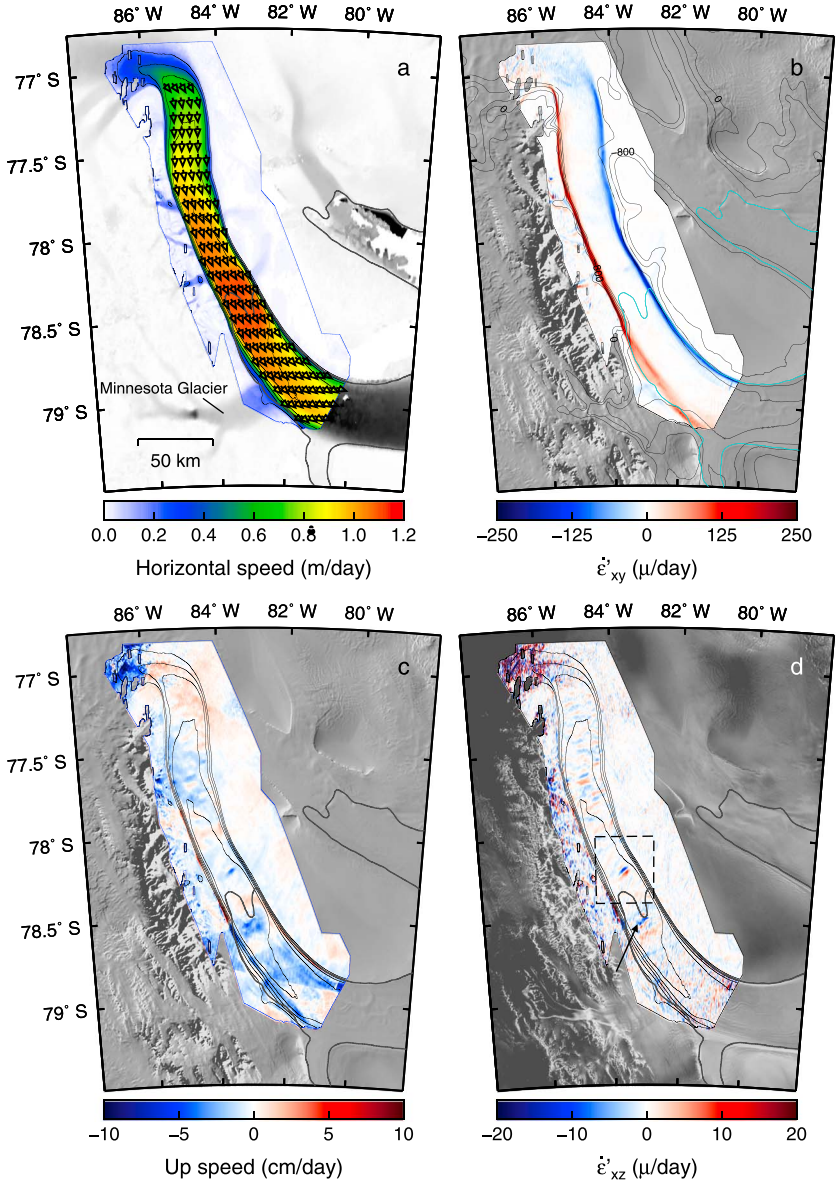


**Figure 5.** Secular velocity components and selected strain rates. (a) Horizontal velocity where colors indicate speed, arrows show flow direction, and gray scale background is horizontal speed from *Rignot et al.* [2011a]. Vector lengths are constant and are chosen for clarity. (b) Lateral shear strain rate, filtered over a Gaussian window with a 670 m standard deviation ($6\sigma \approx 2$ ice thicknesses). Gray scale background is Moderate Resolution Imaging Spectroradiometer mosaic of Antarctica 2009 [*Haran et al.*, 2005; *Scambos et al.*, 2007; *Haran et al.*, 2014] and contour lines are bathymetry in 400 m increments [*Fretwell et al.*, 2013]. (c) Vertical velocity, where positive values are moving upward. Gray scale background is the same as Figure 5b, and contour lines are horizontal speed from Figure 5a in 0.2 m/d increments. (d) Along-flow vertical shear strain rate filtered as in Figure 5b. Gray scale background is RADARSAT-1 AMM-1 mosaic [*Jezek et al.*, 2013], and contour lines are the same as Figure 5c. Dashed rectangle shows area of interest in Figure 6. Grounding lines are indicated in all panels by sinuous, dark gray lines and are the same as in Figure 1.

#### 4.1.1. Horizontal Velocity

The inferred horizontal velocity field has characteristics consistent with expected ice stream flow in Antarctica and qualitatively agrees with previously published velocity fields over RIS (e.g., gray scale image in Figure 5a, from *Rignot et al.* [2011a] and differential velocity in Figure S16). Horizontal speeds during the CSK data collection (color map in Figure 5a) range from near zero in the upstream extent of our observational domain to approximately 1.2 m/d in the vicinity of the grounding line. The direction of ice flow, given by the field of arrows in Figure 5a, curves eastward by approximately 45° within our observational domain from almost pure

southerly flow in the upstream region to southeasterly flow in the downstream region. (Note that for clarity the lengths of the arrows in Figure 5a are constant.)

Regions of faster flow lie primarily along the western side of ice stream, largely due to deeper bathymetry and thicker ice abutting and downstream of the Ellsworth Mountains (Figure 1). This westward trend in flow speed is most pronounced within a zone of relatively low horizontal speeds located along the eastern wall of the ice shelf. This zone is defined at the landward extent by a patch projecting approximately a quarter of the local ice stream width into the main trunk (78.7°S, 82.5°W). The patch is located on the upstream side of a prominent high in the bathymetry (white, broken circle in Figure 1d) and adjacent to a known pinning point [*Schmeltz et al.*, 2001]. The relatively low-velocity region extends to the eastern boundary of the data domain and, as we later show, plays an important role in the response of the ice stream flow to tidal forcing. The relatively shallow basal topography and thick ice (Figure 1e) suggest that the shelf grounds in this region during low tide.

#### 4.1.2. Lateral Shear Strain Rate

Lateral shearing ($\dot{\varepsilon}'_{xy} = \frac{1}{2}[\partial v'_x/\partial y + \partial v'_y/\partial x]$, where $x$ is along flow and $y$ is across flow in a right-hand coordinate system that includes the up vector) is strongest in the grounded ice stream margins and diminishes to near zero within the main trunk of RIS (Figure 5b). This strain localization is due to the combination of nonlinear ice rheology and shear heating, damage, and ice fabric reorientation in the margins [e.g., *Echelmeyer et al.*, 1994; *Suckale et al.*, 2014; *Hudleston*, 2015; *Perol and Rice*, 2015]. Lateral shear rates are high where the ice stream is bounded by steep bathymetry, with maximum values located in areas where bathymetry is steepest along both the east and west margins. Shearing is relatively low in the upstream eastern margin, where bathymetric slopes are shallow, and in the ice shelf margins. The lowest shear strain rates within the margins are coincident with the suture zone where Minnesota Glacier (MG) intersects RIS. Shearing increases, relative to its upstream value, as ice approaches the nunatak at 79.3°S, 81.5 °W. The first-order thicknesses of the shear margins vary as the inverse of the shear strain rate such that the thinnest shear margins contain the highest secular horizontal speeds, consistent with stress balance.

#### 4.1.3. Vertical Velocity and Shear Strain Rate

Secular vertical velocity is near zero over most of the observational domain (Figure 5c). Given the shallow surface slope on RIS, these inferred vertical speeds are broadly consistent with those expected for along-slope flow. The notable exception of zero velocity is the large triangular zone of downward motion over the ice shelf, where inferred downward motion is caused primarily by relatively high covariances between the secular horizontal and vertical velocities (Figure S17). These covariances are driven by nonideal viewing geometries in the CSK tracks that cover this region (see supporting information Text S2 for further discussion). While the values of up velocity over large scales are consistent with along-slope flow, high-frequency variations provide some relevant details about the response of ice stream flow to variations in bathymetry beneath grounded ice and the mechanical properties of the ice-bed interface (Figures 5c and 5d).

The most prominent high-frequency feature in the vertical velocity is located approximately 40 km upstream of the grounding line, within the main trunk of RIS (Figure 6). This patch, characterized in our SAR-derived velocity fields by high horizontal velocity divergence and a doublet in the along-flow vertical shear strain rate, is within 10 km (~5 ice thicknesses) downstream of an area known to contain localized stiff basal sediments and a prominent bathymetric ridge [*King et al.*, 2009; *Smith and Murray*, 2009; *Smith et al.*, 2015; *King et al.*, 2016]. To the east and west of the ridge are troughs filled with saturated, deforming sediments. The surface slope, as found in high resolution, GPS-derived surface topography [*King et al.*, 2016], is exceptionally steep within a small surface patch, further indicating a significant, localized increase in basal shear traction. As we discuss later, the presence of this near-centerline bathymetric ridge and high in basal shear traction has a notable influence on how velocity variations at tidal timescales are propagated through the grounded ice stream.

In the vicinity of the grounding zone, we observe upstream thickening and downstream thinning (Figures 5c and 5d). Thickening occurs landward of the bathymetric high located within the central trunk of the ice stream that causes the grounding line to take on a U shape. Once ice crosses the grounding zone, localized thinning results in observed downward surface velocity.

### 4.2. Periodic Deformation Fields

A unique contribution of this analysis is the quantification of time-dependent velocity. Here we present the salient sinusoidal amplitude and phase values, beginning with the vertical (forcing) components. Formal error estimates are given in the supporting information Text S2.

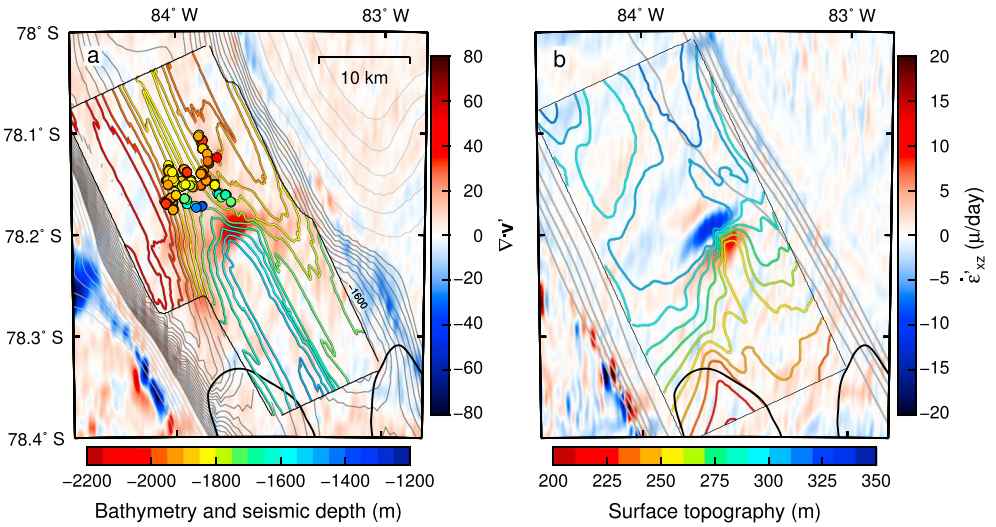


**Figure 6.** Influence of bathymetry and basal mechanics on observed surface velocity fields. (a) Divergence of surface velocity (color map), assuming negligible $\dot{\varepsilon}_{zz}$, in the area of interest outlined in Figure 5d. Colored contour lines show detailed bathymetry in 50 m increments from *King et al.* [2016], while colored dots show seismic event locations from *Smith et al.* [2015]. Thin gray contour lines are bathymetry from Bedmap2 in 50 m increments below −1200 m (dark gray) and 200 m increments above −1200 m (light gray). (b) Along-flow vertical shear strain rate (color map) with surface elevation in 10 m increments (colored contour lines) [*King et al.*, 2016]. Gray contour lines are horizontal speed from Figure 5a in 0.2 m/d increments. Grounding lines (heavy black lines in both panels) are the same as in Figure 1.

#### 4.2.1. Vertical Motion

The $M_2$ and $O_1$ tidal constituents have the largest vertical amplitudes of all the tidal frequencies that are observable with CSK, while the $M_{sf}$ amplitude is relatively negligible [*Padman et al.*, 2002; *Padman and Fricker*, 2005]. We therefore discuss results only at $M_2$ and $O_1$ frequencies for brevity, but note that the inferred $M_{sf}$ amplitudes are in good agreement with modeled values from CATS2008a_opt over the ice shelf [*Padman and Fricker*, 2005] and are near zero over grounded ice, consistent with GPS observations [*Gudmundsson*, 2006; *Murray et al.*, 2007]. We further note that it is not possible to directly observe periodic grounding in the inferred vertical fields because we assumed all variations were sinusoidal and grounding is likely better represented by a sinusoid clipped at a minimum value equal to the depth below mean sea level at which the ice shelf grounds. We will address this potential shortcoming in future work.

##### 4.2.1.1. Lunar Semidiurnal Component

Vertical $M_2$ amplitude and phase values are broadly consistent across the central trunk of the ice stream (Figures 7a and 7b and Movie S1) and are in good agreement with the CATS2008a_opt regional tidal model, whose predicted tidal amplitudes fit colocated GPS observations [*Padman et al.*, 2002; *Padman and Fricker*, 2005; *Gudmundsson*, 2006]. Amplitudes decrease quickly in the vicinity of the grounding zone, while the respective phase values—in areas with amplitudes high enough to give reasonable phase estimates—lag ($< 0$) by approximately 20 min in most areas within 10 km of the grounding zone. Phase lag within the grounding zone is most prevalent and has the largest areal extent within the two horns that mark the immediate downstream side of the grounding zone of RIS. Comparing the two horns, we observe roughly symmetric phase values and asymmetric amplitudes, where amplitudes in the western horn are a factor of 2 larger than in the eastern horn. Landward of the grounding zone, we observe zero amplitude for the $M_2$ component.

##### 4.2.1.2. Lunar Diurnal Component

Vertical $O_1$ amplitude and phase values have greater spatial variability than $M_2$ values but are in broadly good agreement with CATS2008a_opt predictions (Figures 7c and 7d). As with $M_2$ amplitudes, $O_1$ amplitudes decrease rapidly within approximately 10 km of the grounding zone and are near zero over grounded ice. As with $M_2$, leading phase values are located at the pinning point studied by *Schmeltz et al.* [2001] (black arrow in Figure 7d).

#### 4.2.2. Horizontal Fields

Low-frequency ($M_{sf}$; 14.77 day period) variations are dominant in horizontal ice flow [*Gudmundsson*, 2006, 2011; *Murray et al.*, 2007, 2006; *Aðalgeirsdóttir et al.*, 2008]. GPS observations at 40 km upstream of the

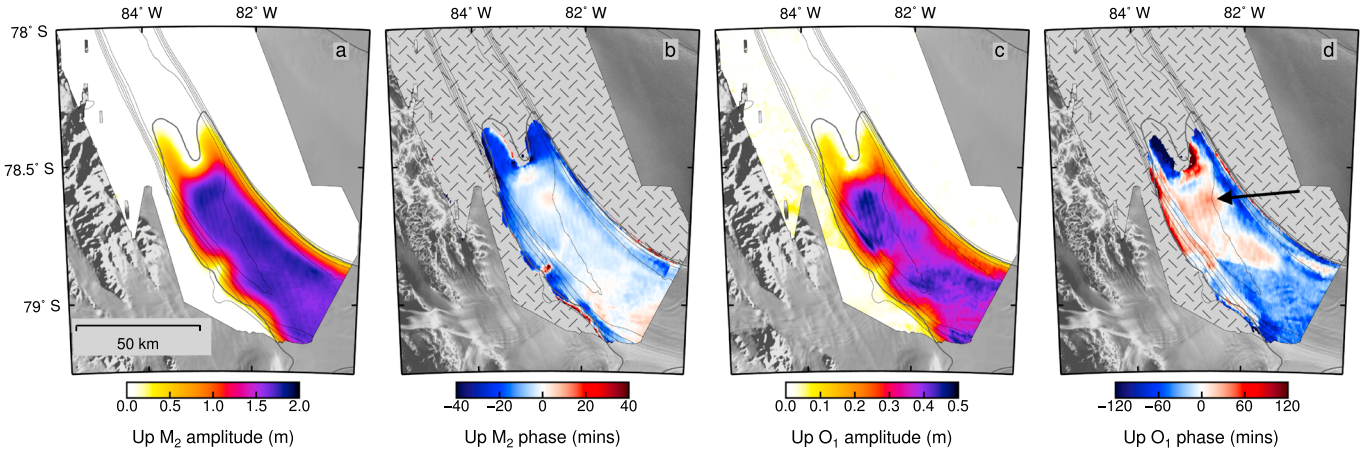


**Figure 7.** Time-dependent vertical displacement components for $M_2$ lunar semidiurnal and $O_1$ lunar diurnal tidal periods (Figures 7a–7d). (a) Vertical amplitude for the $M_2$ tide with dark, thin contour lines showing horizontal secular speed in 0.2 m/d increments. (b) Vertical $M_2$ phase relative to the median $M_2$ phase over the ice shelf. Areas with amplitude < 10 cm are crosshatched for clarity. (c and d) Same as Figures 7a and 7b but for $O_1$ values. Grounding lines are the same as in Figure 1.

grounding line show that horizontal amplitudes at $M_2$ and $O_1$ frequencies are more than an order of magnitude smaller than at $M_{sf}$, with both $M_2$ and $O_1$ characterized by subcentimeter-scale amplitude variations. For brevity and due to the disparity in amplitudes, we discuss only results for the horizontal component of $M_{sf}$ period variations. We note that inferred $M_2$ and $O_1$ amplitudes are more than an order of magnitude smaller than $M_{sf}$ amplitudes in the areas of interest, consistent with GPS observations.

#### 4.2.2.1. Along-Flow Periodic Variations

Inferred along-flow amplitudes at the $M_{sf}$ period over grounded ice are highest near the grounding zone and diminish with distance upstream (Figure 8a and Movie S2). Beyond 85 km upstream of the grounding zone, along-flow tidal variability at the $M_{sf}$ period is negligible. It takes approximately 3 days for the signal to propagate 85 km inland (Figure 8b). There is less cross-flow variability than along-flow variability in amplitude and phase values. But as with horizontal speed, the largest amplitudes are located on the deeper western side of RIS.

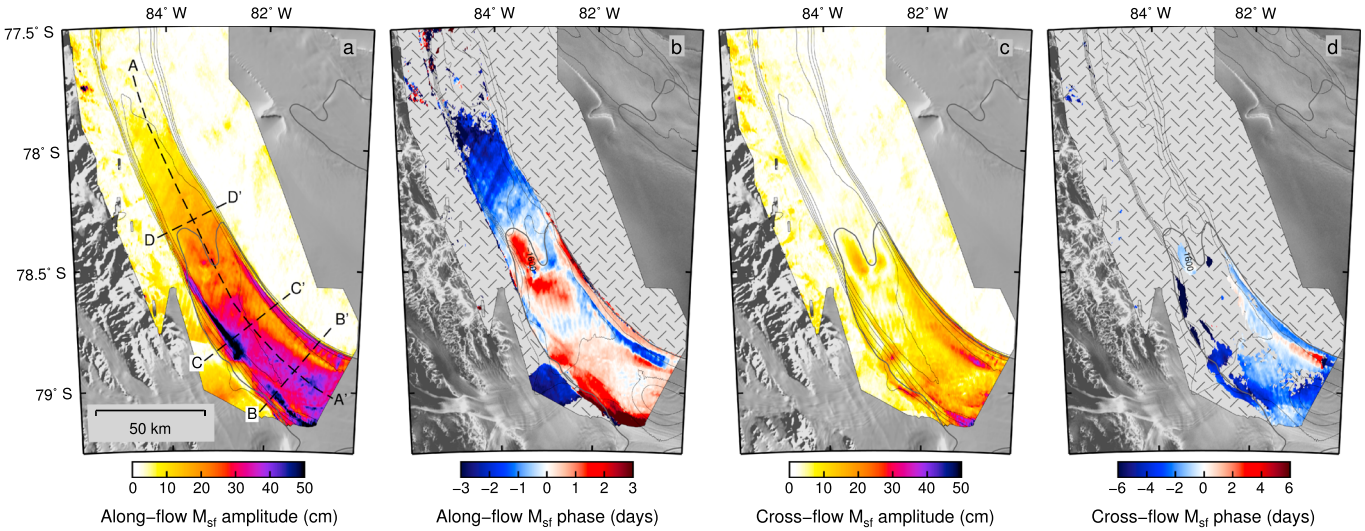


**Figure 8.** Time-dependent along-flow and cross-flow horizontal velocity components for the $M_{sf}$ (14.77 day) tidal period (Figures 8a–8d). (a) Along-flow amplitude with contour lines showing horizontal secular speed in 0.2 m/d increments. (b) Along-flow phase relative to the median along-flow $M_{sf}$ phase over the ice shelf. Contour lines are bathymetry below −1200 m from Bedmap2 in 200 m increments. Areas with small amplitude and horizontal secular velocity are crosshatched for clarity. (c–d) Same as Figures 8a and 8b but for cross-flow variability. Phase values in Figure 8d are referenced to the median along-flow $M_{sf}$ phase over the ice shelf as in Figure 8b. Grounding lines are the same as in Figure 1.

Amplitudes are highest over the ice shelf, where they are spatially heterogenous. Along-flow amplitudes increase smoothly across the grounding zone within the central trunk and are, over much of the ice shelf, at least double the amplitudes at the grounding zone. The largest amplitudes in the observational domain are located along the southwest ice stream margin upstream from where MG intersects RIS and where there is likely to be low-viscosity ice advected from upstream [*Minchew*, 2016]. High amplitudes are also present at the extreme downstream end of the observational domain in the vicinity of a known deep bathymetric trough (Figure 1d). Some of the lowest amplitudes over the ice shelf are located along the eastern margin, where shallowing bathymetry likely causes the ice stream to ground during low tide.

In general, the ice shelf leads the grounded ice in tidal response. Leading (positive) phase values are present along much of the ice stream trunk. Among the first areas to accelerate is the downstream portion of the western grounding zone horn, where some of the thickest ice, supported by the deepest bed under RIS, goes afloat. This horn provides the wider of two passages between the bathymetric channel sidewalls and the central ridge that pins the grounding line at the downstream extent of the U-shaped bend and features larger vertical uplift at $M_2$ and $O_1$ periods than the eastern horn. Leading phase values extend downstream from the western horn into the central trunk. Leading phase values are also present in the downstream extent of the central trunk. Lagging phase values are manifest near the eastern shelf margin, where we observe relatively slow secular ice flow. MG experiences tidal variability with approximately the same amplitude as upstream areas on RIS but lags variations on the ice shelf by 3 days or more. We observe no clear spatial correlation between amplitude and phase values within the observational domain.

#### 4.2.2.2. Cross-Flow Periodic Variations

The margins of RIS are largely constrained by bathymetry, causing the flow direction to remain approximately constant, the $M_{sf}$ cross-flow amplitude to be near zero, and the cross-flow phase to be approximately constant over most of the observational domain (Figures 8c and 8d). Significant cross-flow variations occur on both the east and west sides of the U-shaped grounding line bend, with most of the cross-flow variations occurring in the western horn. But the largest cross-flow variations occur near or within the ice shelf margins and predominantly near the downstream extent of the observational domain. Cross-flow amplitude increases markedly at the intersection of MG and RIS. A localized region containing the highest cross-flow amplitudes is manifest near the eastern shelf margin at the downstream extent of the observational domain. This feature is coincident with a relative low in along-flow amplitude, slow secular horizontal velocity, and shallowing bathymetry. Taken together, these observations suggest that the ice shelf grounds along the eastern margin at low tide.

#### 4.2.2.3. Propagation of Tidal Signals

Inferred along-flow $M_{sf}$ period amplitude and phase values agree with colocated GPS measurements (Figure 9) [*Gudmundsson*, 2006; *Murray et al.*, 2007; *Aðalgeirsdóttir et al.*, 2008]. Longitudinal $M_{sf}$ period flow variability propagates upstream of the grounding zone at a mean rate of approximately 24.3 km/d within the first 30 km and at a faster mean rate of 34.3 km/d between 40 and 80 km upstream of the grounding zone. Amplitudes in along-flow $M_{sf}$ variability diminish quasi-linearly with distance at approximately 2.6 mm/km over 85 km upstream (Figures 8a and 8b and 9). Despite pointwise agreement between the SAR-derived and GPS-measured $M_{sf}$ amplitude and phase values, propagation and damping rates are notably different. Estimates of upstream $M_{sf}$ along-flow propagation are slower in the CSK-inferred fields relative to speed estimated from GPS data by *Gudmundsson* [2006] but agree with estimates from data presented by *Murray et al.* [2007]. Damping rates are consistent with both GPS studies but are slightly higher than those inferred by *Gudmundsson* [2006] from four GPS stations located along the central flow line. The most likely explanation for disparities between our estimates and those of *Gudmundsson* [2006] is the limited duration and the season of the GPS data collection. The colinear GPS data were collected for approximately 2 months during the 2003–2004 austral summer. The limited duration of the data makes it impossible to separate from the $M_{sf}$ (14.77 day period) component contributions from the lunar fortnightly, $M_f$ (13.66 day period) and lunar monthly, $M_m$ (27.55 day period), tides, which have similar periods to and whose amplitudes are within an order of magnitude of $M_{sf}$. Two months is also too short to allow for inferences of the strong seasonal and annual variability on RIS, which reach a minimum during the austral summer [*Murray et al.*, 2007]. CSK observations spanned approximately 9 months, and though we are unable to uniquely infer annual, seasonal, $M_f$, and $M_m$ variability, we show in the synthetic results that our sampling rate is sufficient to solve for accurate solutions for $M_{sf}$ alone (see supporting information Text S1 for more details).

Along-flow $M_{sf}$ period amplitude and phase values display sensitivities to the mechanics of the ice-bed interface and ice thickness (Figure 9). The most distinct manifestation of this sensitivity occurs at the downstream

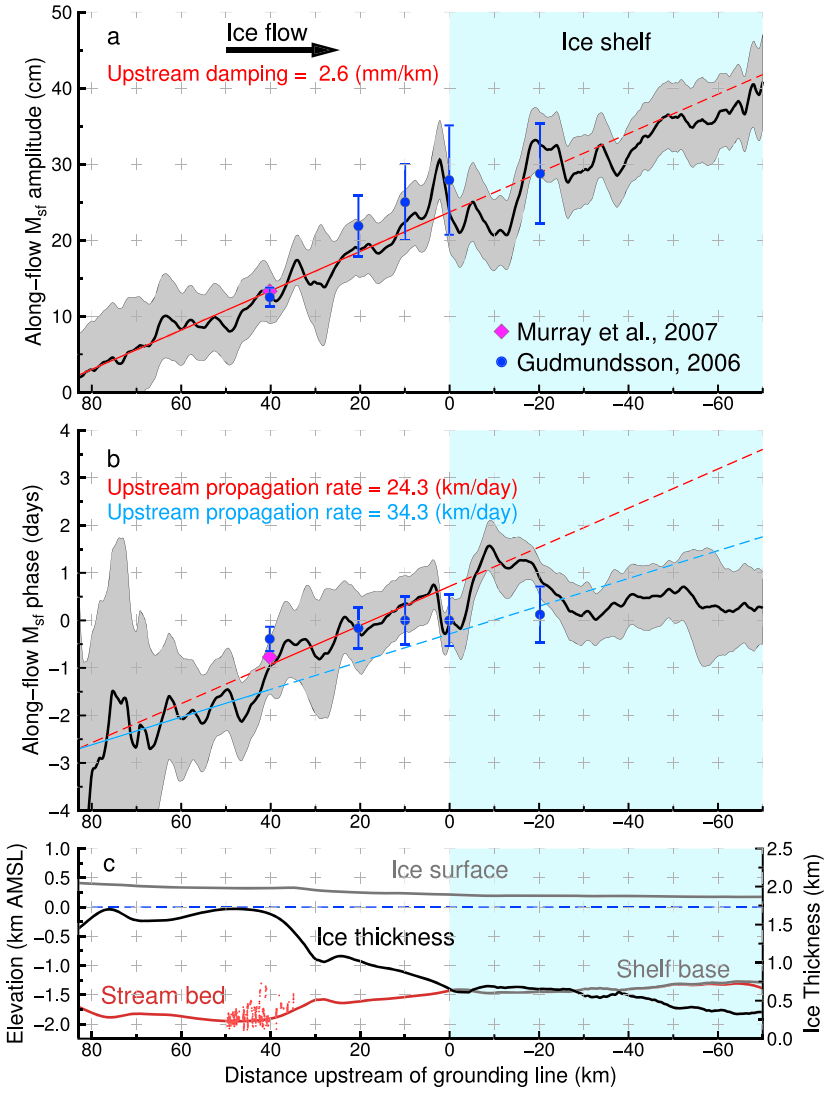


**Figure 9.** Longitudinal $M_{sf}$ (a) amplitude and (b) phase values along centerline transect A–A′ with colocated, noncontemporaneous GPS observations from *Murray et al.* [2007] (magenta diamond) and *Gudmundsson* [2006] (blue circles). Gray shaded region around the lines and error bars on the GPS data indicate 2 standard deviations about the measured value. Linear trends are fit to areas where the respective line is solid and extrapolated in dashed lines for reference. Red line indicates propagation for the first 40 km upstream of the grounding line, and the blue line shows the propagation for 40–80 km upstream. (c) Collocated ice stream geometry from Bedmap2 overlain by red dots indicating the projection of seismic event locations from Figure 6a onto the transect. Light blue shaded regions in all panels indicate floating ice.

extent of the grounding zone, where the ice detaches from the centerline ridge (0 km in Figure 9). At this point there are sharp increases in amplitude and phase lags, relative to the respective upstream and downstream values. Inland of the grounding zone, this sensitivity is most distinct between 30 and 40 km inland, where the ice stream encounters a prominent centerline ridge (Figure 6). In this area, phase lags by more than a day and amplitude decreases by approximately 25% landward of the ridge where centerline bathymetry is deepest. This deep section corresponds to the region with higher $M_{sf}$ period propagation speeds.

## 5. Discussion

Time-dependent velocity fields illuminate the spatially complex response of horizontal ice flow to ocean tidal motion. Because these are the first ice stream-scale inferences of spatiotemporal variations in vertical and horizontal ice motion, our goal here is to discuss the principle results, leaving more detailed analysis of

individual processes for subsequent studies. The arc of this discussion begins over the ice shelf—the source of the forcing—and proceeds upstream.

### 5.1. Flow Variations Over the Ice Shelf

$M_{sf}$ period variations in horizontal velocity over the ice shelf drive variations at the same frequency within and upstream of the grounding zone. This conclusion is supported most clearly by the observation that the ice shelf responds first (leading phase values) and most strongly (highest amplitudes), relative to the ice stream, at the $M_{sf}$ period. Broadly speaking, $M_{sf}$ period amplitude increases with distance downstream (seaward) of the grounding zone while the RIS-bisecting grounding zone transition can be roughly characterized as a multiday step in the timing of ice-flow response (phase). Whether the driver of leading phase and increasing amplitudes is distal—through transmission of stress perturbations from the main body of FRIS [*Makinson et al.*, 2012]—or proximal to the observational domain remains an open question that could be addressed with observations covering the bulk of FRIS. But what our observations indicate is that variations in ice flow at tidal timescales are enabled, but not driven, by migration of the RIS-bisecting section of the grounding zone, as further evident in the spatial characteristics of vertical and horizontal ice shelf response.

Vertical ice shelf motion is well described as spatially homogenous within the central trunk (i.e., seaward of the flexure zone), while horizontal flow variability is spatially heterogenous over the ice shelf. Within the central trunk, near-constant amplitude and phase values at $M_2$ and $O_1$ show that the observed ice shelf rises and falls monolithically, whereas different sections of the ice shelf experience variations in ice flow that may be more than a factor of 2 higher or lower than other parts of the ice stream. This basic observation is potentially at odds with assumptions of a simple, buoyancy-driven horizontal forcing over the ice shelf generated by vertical tidal motion. In other words, the stark disparity in the spatial characteristics of vertical tidal motion ($M_2$ and $O_1$ amplitude and phase) and horizontal flow response (primarily along-flow $M_{sf}$ amplitude and phase) means that the fundamental forcing function over the ice shelf is unlikely to be linear with tidal height. As an alternative, we propose that periodic grounding along the ice shelf margins translates vertical tidal motion into observed horizontal flow variability.

Regions of the ice shelf that exhibit some of the highest amplitudes and leading phase values are located near periodic grounding zones along the ice stream margins. Periodic grounding is evident in changes in the characteristics of lateral shear strain rate (Figure 10). Assuming negligible normal stresses and considering only fortnightly and shorter timescales, an ice shelf has a vertically integrated lateral shear strain rate profile defined as follows:

$$\dot{\varepsilon}_{xy}(y,t) = \frac{\dot{\tau}_{xy}(y,t)}{E(y)} + \frac{1}{2h(y)\eta(y)} \int \left[\tau_b(y,t) - \tau_d(y)\right] \mathrm{d}y \tag{29}$$

where $E(y)$ is Young's modulus for ice, $h(y)$ is ice thickness, $\eta(y)$ is depth-averaged effective dynamic ice viscosity, $\tau_b(y,t)$ is basal shear traction, $\tau_d(y)$ is gravitational driving stress, $\dot{\tau}_{xy}(y,t) = \partial\tau_{xy}(y,t)/\partial t$ is the rate of change of lateral shear stress, and $x$ and $y$ are along- and cross-flow coordinates, respectively (Appendix B). In general, $\dot{\varepsilon}_{xy}(w) = 0$ (where $y = w$ at the centerline where the terms in equation (29) vary smoothly across flow) is a good assumption and is supported by our observations. While lateral variations in $h$, $\eta$, $\tau_d$, and $\tau_b$ may cause $\dot{\varepsilon}_{xy}$ profiles in real ice shelves to depart from the profiles of idealized viscous ice stream flow [e.g., *Joughin et al.*, 2004], and temporal variations in $\dot{\tau}_{xy}$ and $\tau_b$ will alter the $\dot{\varepsilon}_{xy}$ profile in time, the only plausible driver of change over fortnightly timescales is temporal variations in $\tau_b$. As a result, the evolution of $\tau_b$ at a given position and time can change the shape of the lateral shear strain rate profile at the $M_{sf}$ period (Appendix B). Such changes in the location of maximum lateral shear strain rate and the shape of the lateral shear strain rate profiles are observed near the margins of the ice stream, coincident with shallowing bathymetry, indicating temporal variations in $\tau_b$ caused by periodic grounding over the $M_{sf}$ period tidal cycle (Figures 10a–10f). Note that in the ice stream, where $\tau_b$ is likely to be approximately constant over the timescales of interest [e.g., *Kamb*, 1991; *Tulaczyk et al.*, 2000a, 2000b], lateral shear strain rates increase and decrease in the margins as ice flow varies but do not change their characteristic shape nor the location of maximum shear strain rates (Figures 10g–10i).

The effect of periodic grounding at ice shelf margins is to cause the shear margins to migrate. This migration changes the effective width of the ice shelf, which has a marked influence on ice flow. While the changes we observe are complicated, it is possible to gain some intuition into the sensitivity of ice flow to changes in width by considering an idealized, confined ice shelf, where ice rheology, $h$, and $\tau_d$ are taken to be constant

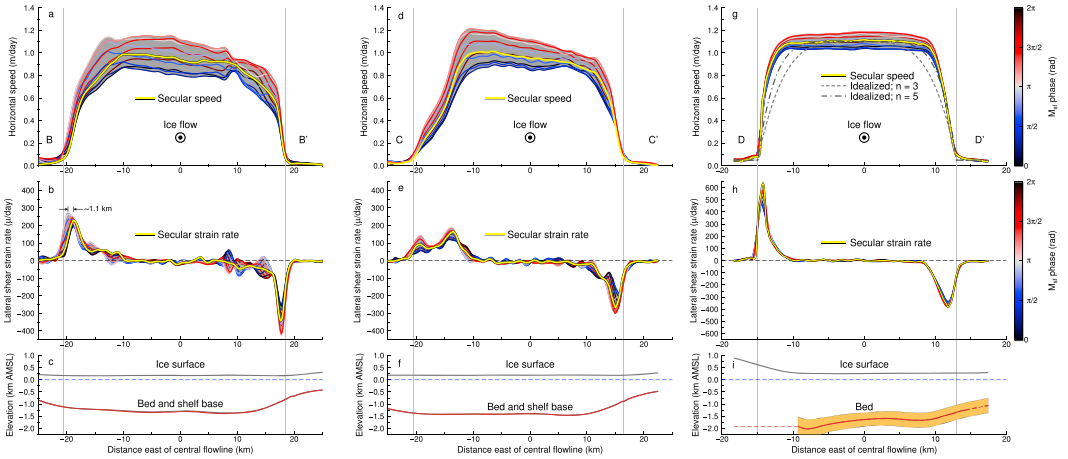


**Figure 10.** Time-dependent horizontal flow, time-dependent lateral shear strain rate, and ice stream geometry along transections (a–c) B–B′, (d–f) C–C′, and (g–i) D–D′ (shown in Figure 8a). In all cases, ice flow direction is out of the page. Line colors and gray shaded regions indicate 1 $M_{sf}$ period cycle, and geometric data are from Bedmap2. Gray dashed and dash-dotted lines in Figure 10g show an idealized ice stream profile for $n = 3$ and $n = 5$, respectively. Dashed brown line in Figure 10i indicates that no bathymetric data are available within 3 km in any direction and shows the bed profile for the model geometry, while light brown shaded region gives the 2 standard deviation uncertainty in bathymetry.

across the flow and $\tau_b = 0$ everywhere [e.g., *Raymond*, 1996]. Taking $w$ to be the half width of the ice shelf and ignoring the elastic component of ice rheology for simplicity, it can be shown (Appendix B) that the centerline velocity in the idealized ice shelf is given as follows:

$$v_{\text{center}} = \frac{2A}{n+1}\left(\frac{\tau_d}{h}\right)^n w^{n+1} \tag{30}$$

where $A$ is the rate factor and $n$ the exponent in Glen's Flow law [*Glen*, 1955; *Cuffey and Paterson*, 2010]. The nonlinear dependence of centerline velocity on width could give rise to the nonlinear response of horizontal ice flow to vertical tidal motion [e.g., *Gudmundsson*, 2006, 2011]. Furthermore, migration distance and residence time depends on the characteristics of tidal uplift and will therefore exhibit seasonal variability as observed by *Murray et al.* [2007].

### 5.2. Upstream Propagation

Variations in ice flow over the ice shelf are communicated through the grounding zone and to a maximum of 85 km inland across the entire width of RIS. At the $M_{sf}$ period, the elastic properties of ice play an important role in stress transmission [*Gudmundsson*, 2011; *Thompson et al.*, 2014; *Rosier et al.*, 2014]. Our observations indicate that upstream stress transmission only occurs once the ice accelerates along the entire RIS-bisecting grounding zone. This conclusion is evident in the along-flow, $M_{sf}$ period phase map where inferred phase values show that while the western horn of the grounding zone accelerates days before the ice stream, the timing of ice stream accelerations is coincident with those of the central grounding zone (where the high bathymetric ridge is located) and the eastern grounding zone horn. The downstream extent of the grounding zone features relatively strong along-flow vertical shear strain rate (black arrow in Figure 5d), meaning that unpinning from this point is likely necessary for upstream transmission of stresses from the ice shelf. Given that inferred phase values at this point lag most of the ice shelf and the $M_{sf}$ period amplitudes are smaller than over most of the ice shelf, unpinning from this point on the grounding zone is not sufficient to explain the observed variations in ice flow.

The upstream propagation of stress changes is influenced by basal mechanics and ice thickness. This dependence is most evident along the centerline of the ice stream at 40 ± 10 km upstream of the grounding zone. In this region, there is a seismically active transition from dilatant to stiff sediment [*Smith et al.*, 2015] and a steep ice thickness gradient [*King et al.*, 2016]. Because observed ice flow on RIS is primarily facilitated by basal slip [e.g., *Morlighem et al.*, 2013], the upstream propagation velocity of variations in ice should scale with the square root of ice thickness and basal shear traction [*Rosier et al.*, 2014], which is consistent with our observations.

However, for variations in ice flow to propagate to 85 km upstream, the margins of RIS must be weak relative to the central ice [*Thompson et al.*, 2014]. Marginal weakening is likely to occur through shear heating in areas with high, localized strain rates [e.g., *Echelmeyer et al.*, 1994; *Suckale et al.*, 2014; *Perol and Rice*, 2015], such as those observed in margins upstream of the RIS grounding zone. While a thorough examination of marginal weakening is beyond the scope of this study, we use the idealized flow model from equation (30), but with $\tau_b > 0$ and assuming $\tau_b/\tau_d$ is constant across the flow (Appendix B), to calculate the profile of horizontal velocity at a representative ice stream transect (Figures 10g–10i). Profiles calculated for $n = 3$ and $n = 5$ show that the model is a poor fit to the observations within the range of reasonable values of $n$ [*Goldsby and Kohlstedt*, 2001]. Due to the assumption that $A$ is spatially constant, these results represent the case where the margins are as strong as the central ice stream. Therefore, while further work is warranted, the observed velocity fields provide strong evidence that the margins of RIS are weakened by shear heating and that this weakening is likely sufficient to allow for transmission of stresses from the ice shelf to the distances observed [*Minchew*, 2016]. Downstream advection of weakened marginal ice also accounts for the high $M_{sf}$ period along-flow amplitudes seen in the western shelf margins, though further work is needed to model the influence of spatial gradients in ice viscosity on $M_{sf}$ period flow variability.

### 5.3. Further Methodological Development

In addition to future mechanistic studies discussed above, our results motivate further work on the observational methodology. Here we contribute the first ever time-dependent, 3-D velocity fields of an entire ice stream and its proximal ice shelf. We chose RIS as the study area because it provides opportunities to study unique processes discussed previously and a relatively simple proof-of-concept subject for developing the observational methodology. GPS observations have been collected on RIS, which has been relatively stable over the observational record, allowing us to focus on the special case where the displacement of the ice surface can be described by a secular velocity and a family of sinusoidal terms whose periods are constrained by the GPS observations. This combination of relatively simple temporal variability and extensive, high-quality observations is extraordinary. In other areas, the special case of sinusoidal variability will break down due to transient or other nonsinusoidal acceleration [e.g., *Rignot*, 1998b; *Scambos et al.*, 2004; *Joughin et al.*, 2012b; *Mouginot et al.*, 2014], and independent observations useful for constraining the temporal basis functions a priori may not exist. To address these shortcomings, a more general description of time-varying ice flow will need to be implemented in multiple spatial dimensions along with algorithms to constrain the solution space [e.g., *Riel et al.*, 2014]. Constraining the solution space is crucial for computational tractability and for generating viable inferences of ice flow from a time series of remotely sensed observations. Building upon the methodology presented here will leverage existing and future remote sensing data sets to facilitate a more profound understanding of the spatiotemporal characteristics of glacier flow, further challenging ice flow models and helping to illuminate the mechanisms responsible for observed glacier flow variability.

## 6. Conclusions

We present a method for inferring time-dependent, 3-D surface velocity fields from continuous SAR and optical remote sensing observations, focusing on the special case where ice flow can be described with a 3-D secular velocity and a family of 3-D sinusoidal functions. The inferred velocity fields are the first to quantify synoptic-scale, time-varying response of ice stream flow to tidal timescale forcing and thereby represent a new step in the development of geodetic methods aimed at a mechanistic understanding of glacier flow. Essentially, we have combined some of the temporal benefits of GPS data with the spatial benefits of remote sensing to illuminate the spatiotemporal characteristics of ice flow in RIS. Our focus on the special case of sinusoidal variability and the need to prescribe the periods of sinusoidal variability motivates further work to generalize the approach to include a variety of temporal functions and methods to eliminate dependence on a priori knowledge of the temporal basis functions.

Our results over RIS, where the aforementioned special case holds, indicate that the strongest variability in horizontal ice flow occurs at the $M_{sf}$ (14.77 day) period over the ice shelf, where amplitudes exceed those of grounded ice by up to a factor of 3. The inferred $M_{sf}$ period along-flow variability propagates upstream at a mean rate of 24.3 km/d within 30 km of the grounding zone and 34.3 km/d between 40 and 80 km upstream of the grounding zone. Along the way, the signal amplitude is damped by 2.6 mm/km and is almost completely damped beyond 85 km upstream of the grounding zone. Propagation rates and amplitudes of $M_{sf}$ along-flow variability are sensitive to basal mechanics and ice thickness, with the most notable alterations in amplitude

and phase occurring at the seismically active, upstream side of a prominent, near-centerline, bathymetric ridge. We show that the margins of RIS are weakened due to shear heating, likely a necessary condition for propagating stress variations from the ice shelf to over 85 km inland.

Relatively high amplitudes in horizontal flow variability and leading phase values over the ice shelf show that ice shelf motion drives observed changes in ice stream flow. Moreover, vertical motion over the ice shelf is spatially homogeneous, while horizontal flow variability is spatially heterogenous. Based on these observations, we propose that the primary mechanism for translating vertical motion of the RIS ice shelf into horizontal flow variability is periodic grounding of the ice shelf. Periodic grounding is most important near the margins, where sloping bathymetry results in an effective widening of the ice shelf at tidal frequencies, allowing for faster flow. Periodic grounding is not currently considered in models of tidal variability and should help to improve our understanding of how ice tides, and, more generally, changes in stress over ice shelves, influence ice stream flow.

## Appendix A: Errors in Inferred Topographic Residuals

When considering whether to estimate topographic residuals, it is important to consider the total error and error components in $\delta z_d$. From equation (11), the error in residual topographic signals is given as follows:

$$\begin{aligned}\sigma^2_{\delta z_d} &= \left(\frac{\partial \delta z_d}{\partial b_{ab}}\right)^2 \sigma^2_{b_{ab}} + \left(\frac{\partial \delta z_d}{\partial B_{\perp_{ab}}}\right)^2 \sigma^2_{B_{\perp_{ab}}} + \left(\frac{\partial \delta z_d}{\partial r_0}\right)^2 \sigma^2_{r_0} + \left(\frac{\partial \delta z_d}{\partial \theta_0}\right)^2 \sigma^2_{\theta_0} \\ &= \left(\frac{r_0 \sin\theta_0}{B_{\perp_{ab}}}\right)^2 \sigma^2_{b_{ab}} + \left(\frac{b_{ab} r_0 \sin\theta_0}{B^2_{\perp_{ab}}}\right)^2 \sigma^2_{B_{\perp_{ab}}} + \left(\frac{b_{ab}\sin\theta_0}{B_{\perp_{ab}}}\right)^2 \sigma^2_{r_0} + \left(\frac{b_{ab} r_0 \cos\theta_0}{B_{\perp_{ab}}}\right)^2 \sigma^2_{\theta_0}.\end{aligned} \tag{A1}$$

To illustrate the sensitivity of $\delta z_d$ to measurement noise, let us assume accurate orbital positions such that $\sigma^2_{B_{\perp_{ab}}} \approx \sigma^2_{r_0} \approx \sigma^2_{\theta_0} \approx 0$. This assumption simplifies equation (A1) such that

$$\sigma_{\delta z_d} \approx \frac{r_0 \sin\theta_0}{B_{\perp_{ab}}} \sigma_{b_{ab}} \tag{A2}$$

where, from equation (2), we have the following:

$$\begin{aligned}\sigma^2_{b_{ab}} &= \left(\frac{\partial b_{ab}}{\partial d_{ab}}\right)^2 \sigma^2_{d_{ab}} + \left(\frac{\partial b_{ab}}{\partial \Delta u^*_{ab}}\right)^2 \sigma^2_{\Delta u^*_{ab}} + \left(\frac{\partial b_{ab}}{\partial \epsilon_{ab}}\right)^2 \sigma^2_{\epsilon_{ab}} \\ &= \left(\Delta u^*_{ab} + \epsilon_{ab}\right)^2 \sigma^2_d + \left(d_{ab} - \epsilon_{ab}\right)^2 \sigma^2_{\Delta u^*_{ab}} + \left(d_{ab} - \Delta u^*_{ab}\right)^2 \sigma^2_{\epsilon_{ab}}\end{aligned} \tag{A3}$$

where $\Delta u^*_{ab} = \hat{\boldsymbol{\ell}} \cdot (\mathbf{u}_a - \mathbf{u}_b)$ (equation (3)). SAR systems always have oblique LOS geometries such that $20° < \theta_0 < 65°$, and their flight paths are constrained to minimize $B_{\perp_{ab}}/r_0$ so that InSAR measurements are more sensitive to target motion than to topography. Therefore, for spaceborne and airborne SAR platforms, $r_0 \sin\theta_0 / B_{\perp_{ab}} \sim 10^3 - 10^4$ [*Rosen et al.*, 2000; *Hensley et al.*, 2009a, 2009b]. To ensure meter-scale precision in estimates of residual topographic signals, it is necessary that $\sigma_{b_{ab}} \lesssim 10^{-3}$ m. This condition is likely to be met only when the signal-to-noise ratio (SNR) is high ($\epsilon_{ab} \ll \Delta u^*_{ab} + b_{ab}$; equation (2)), where the form of $\Delta u^*_{ab}$ is well constrained and where the data allow for accurate estimates of $\Delta u^*_{ab}$. For the foreseeable future, the SNR condition necessitates coherent InSAR data for fine resolution estimates of topographic residuals, excluding many LOS displacement measurements taken from speckle or feature tracking methods, especially for large $\Delta t_{ab}$ in areas with rapid displacement rates [*Bamler and Eineder*, 2005]. If relatively coarse resolution estimates of topographic residuals are acceptable, inferred $\delta z_d$ values can be filtered to reduce $\epsilon_{ab}$ by a factor $\sqrt{N_f}$, where $N_f$ is the number of pixels in the filter window. This will give more accurate estimates of long-wavelength residual topography from LOS displacements when the instrument resolution is sufficiently fine and the displacements are calculated on a sufficiently fine grid to allow for large $N_f$ while maintaining acceptable spatial resolution.

## Appendix B: Idealized Ice Stream

In an idealized ice stream of thickness $h(x, y)$ and half width $w(t)$, ice flows only in the $x$ direction while behaving as an incompressible, Maxwell viscoelastic material with a mass density, $\rho$, which is constant in space

and time. Because the observed velocity at the surface of RIS is approximately equal to the slip rate at the base of the ice [e.g., *Morlighem et al.*, 2013], we adopt the commonly used, vertically integrated shallow-shelf approximation for linear momentum, defined as [*MacAyeal*, 1989] follows:

$$\frac{\partial}{\partial x}\left[h\left(2\tau_{xx}+\tau_{yy}\right)\right]+\frac{\partial}{\partial y}\left(h\tau_{xy}\right)=\tau_b-\tau_d \tag{B1}$$

where $\tau_{ij}$ is the $ij$ element of the deviatoric stress tensor, $\tau_b=\tau_b(y,t)$ is basal shear traction and $\tau_d=\tau_d(y)=-\rho g h\partial h/\partial x$ is the gravitational driving stress ($g$ is gravitational acceleration). Neglecting normal stresses, which is consistent with our observations (Figure S18), simplifies equation (B1) such that

$$\frac{\partial\left(h\tau_{xy}\right)}{\partial y}=\tau_b-\tau_d \tag{B2}$$

or:

$$\tau_{xy}=\frac{1}{h}\int\left[\tau_b-\tau_d\right]\mathrm{d}y \tag{B3}$$

in integral form.

Considering the simplifying assumptions of the model domain described above, the constitutive relation for a Maxwell viscoelastic material is given as follows:

$$\dot{\varepsilon}_{ij}=\frac{1}{E}\frac{\partial\tau_{ij}}{\partial t}+\frac{1}{2\eta}\tau_{ij} \tag{B4}$$

where $E$ is Young's modulus for ice, $2\eta=A^{-1/n}\dot{\varepsilon}_e^{(1-n)/n}$ is the effective dynamic viscosity of ice and $\dot{\varepsilon}_e$ is the effective strain rate (calculated from the second invariant of the strain rate tensor). Rearranging equation (B4) and plugging into equation (B3) gives the following:

$$\dot{\varepsilon}_{xy}=\frac{1}{E}\frac{\partial\tau_{xy}}{\partial t}+\frac{1}{2h\eta}\int\left[\tau_b-\tau_d\right]\mathrm{d}y \tag{B5}$$

which is identical to equation (29).

For the case of pure viscous flow (i.e., where the timescales of interest are much longer than the Maxwell relaxation time $t_r=2\eta/E$), we can neglect the elastic (first) term on the right-hand side of equation (B5). In order to derive the well-known idealized ice stream equation [e.g., *Raymond*, 1996], we further assume that

$$\dot{\varepsilon}_e\approx\dot{\varepsilon}_{xy};\qquad\frac{\partial h}{\partial y}\approx 0;\qquad\frac{\partial\tau_d}{\partial y}\approx\frac{\partial\tau_b}{\partial y}\approx 0. \tag{B6}$$

Incorporating these assumptions and integrating equation (B5) along $y$ yields

$$\dot{\varepsilon}_{xy}=A\left[\frac{w-y}{h}\left(\tau_b-\tau_d\right)\right]^n \tag{B7}$$

under the condition that $\dot{\varepsilon}_{xy}=0$ along the central flow line (i.e., the plane of symmetry) at $y=w$. Recognizing that under the simplifying assumptions of the model

$$\dot{\varepsilon}_{xy}=\frac{1}{2}\frac{\partial v}{\partial y}, \tag{B8}$$

we can integrate equation (B7) along $y$ to arrive at the cross-flow velocity profile defined as follows:

$$v(y)=\frac{2A}{n+1}\left(\frac{\tau_d-\tau_b}{h}\right)^n w^{n+1}\left[1-\left(1-\frac{y}{w}\right)^{n+1}\right] \tag{B9}$$

where we have assumed $v=0$ at $y=0$. Along the centerline, where lateral shearing is negligible, we have the following:

$$v_{\text{center}}=\frac{2A}{n+1}\left(\frac{\tau_d-\tau_b}{h}\right)^n w^{n+1} \tag{B10}$$

which is equivalent to equation (30) when $\tau_b=0$.

**Acknowledgments**
We thank E. Smith and A. Smith for providing the seismic data, and we benefitted from conversations with H. Gudmundsson, H. Martens, V. Tsai, J. Thompson, and P. Agram. B.M. was partially funded by NASA Cyospheric Sciences award NNX14AH80G, NSF Earth Sciences Postdoctoral Fellowship award 1452587, and donations from the Albert Parvin and ARCS LA Chapter foundations. B.R. was partially funded by a NASA Earth and Space Sciences fellowship. P.M. was partially funded by a NASA postdoctoral fellowship, and much of this work was completed while he was a visiting student at the California Institute of Technology. Original COSMO-SkyMed products (copyright ASI—Agenzia Spaziale Italiana, 2013–2016) are archived at JPL and were processed under license from ASI as part of a collaborative project between CIDOT and JPL/Caltech. Displacement fields and other processed SAR data are available from the authors upon request, and the velocity field components will be archived at the National Snow and Ice Data Center (NSIDC; see nsidc.org). Software used to infer time-dependent, 3-D velocity fields is freely available at https://github.com/bminchew/fourDvel.

## References

Aðalgeirsdóttir, G., A. M. Smith, T. Murray, M. A. King, K. Makinson, K. W. Nicholls, and A. E. Behar (2008), Tidal influence on Rutford Ice Stream, West Antarctica: Observations of surface flow and basal processes from closely spaced GPS and passive seismic stations, *J. Glaciol.*, *54*(187), 715–724, doi:10.3189/002214308786570872.

Alley, R. B., S. Anandakrishnan, K. Christianson, H. J. Horgan, A. Muto, B. R. Parizek, D. Pollard, and R. T. Walker (2015), Oceanic forcing of ice-sheet retreat: West Antarctica and more, *Annu. Rev. Earth Planet. Sci.*, *43*(1), 207–231, doi:10.1146/annurev-earth-060614-105344.

Bamler, R., and M. Eineder (2005), Accuracy of differential shift estimation by correlation and split-bandwidth interometry for wideband and Delta-k SAR systems, *IEEE Geosci. Remote Sens. Lett.*, *2*(2), 151–155, doi:10.1109/LGRS.2004.843203.

CSK (2009), COSMO-SkyMed SAR Products Handbook, Italian Space Agency: COSMO-SkyMed Mission, 2nd ed., [Avialable at https://www.e-geos.it/products/pdf/csk-product\%20handbook.pdf.]

Cuffey, K. M., and W. S. B. Paterson (2010), *The Physics of Glaciers*, 4th ed., Elsevier, Amsterdam.

DeConto, R. M., and D. Pollard (2016), Contribution of Antarctica to past and future sea-level rise, *Nature*, *531*(7596), 591–597, doi:10.1038/nature17145.

Doake, C. S. M., H. F. J. Corr, A. Jenkins, K. Makinson, K. W. Nicholls, C. Nath, A. M. Smith, and D. G. Vaughan (2001), Rutford ice stream, Antarctica, in *The West Antarctic Ice Sheet: Behavior and Environment*, vol. 77, edited by R. B. Alley and R. A. Bindschadle, pp. 221–235, AGU, Washington, D. C., doi:10.1029/AR077p0221.

Echelmeyer, K. A., W. D. Harrison, C. Larsen, and J. E. Mitchell (1994), The role of the margins in the dynamics of an active ice stream, *J. Glaciol.*, *40*(136), 527–538.

Emardson, T. R., M. Simons, and F. H. Webb (2003), Neutral atmospheric delay in interferometric synthetic aperture radar applications: Statistical description and mitigation, *J. Geophys. Res.*, *108*(B5), 2231, doi:10.1029/2002JB001781.

Fretwell, P., et al. (2013), Bedmap2: Improved ice bed, surface and thickness datasets for Antarctica, *Cryosphere*, *7*(1), 375–393, doi:10.5194/tc-7-375-2013.

Glen, J. W. (1955), The creep of polycrystalline ice, *Proc. R. Soc. A*, *228*(1175), 519–538.

Goldsby, D. L., and D. L. Kohlstedt (2001), Superplastic deformation of ice: Experimental observations, *J. Geophys. Res.*, *106*(B6), 11,017–11,030, doi:10.1029/2000JB900336.

Goldstein, R. M., H. Engelhardt, B. Kamb, and R. M. Frolich (1993), Satellite radar interferometry for monitoring ice sheet motion: Application to an Antarctic Ice Stream, *Science*, *262*(5139), 1525–1530, doi:10.1126/science.262.5139.1525.

Gourmelen, N., S. Kim, A. Shepherd, J. Park, A. Sundal, H. Björnsson, and F. Pálsson (2011), Ice velocity determined using conventional and multiple-aperture InSAR, *Earth Planet. Sci. Lett.*, *307*(1–2), 156–160, doi:10.1016/j.epsl.2011.04.026.

Gray, A. L., N. Short, K. E. Mattar, and K. C. Jezek (2001), Velocities and flux of the Filchner Ice Shelf and its tributaries determined from speckle tracking interferometry, *Can. J. Remote Sens.*, *27*(3), 193–206, doi:10.1080/07038992.2001.10854936.

Gudmundsson, G. H. (2006), Fortnightly variations in the flow velocity of Rutford Ice Stream, West Antarctica, *Nature*, *444*(7122), 1063–1064, doi:10.1038/nature05430.

Gudmundsson, G. H. (2011), Ice-stream response to ocean tides and the form of the basal sliding law, *Cryosphere*, *5*(1), 259–270, doi:10.5194/tc-5-259-2011.

Gudmundsson, G. H. (2013), Ice-shelf buttressing and the stability of marine ice sheets, *Cryosphere*, *7*(2), 647–655, doi:10.5194/tc-7-647-2013.

Gudmundsson, G. H., J. Krug, G. Durand, L. Favier, and O. Gagliardini (2012), The stability of grounding lines on retrograde slopes, *Cryosphere*, *6*(6), 1497–1505, doi:10.5194/tc-6-1497-2012.

Han, S. C., C. K. Shum, and K. Matsumoto (2005), GRACE observations of M2 and S2 ocean tides underneath the Filchner-Ronne and Larsen ice shelves, Antarctica, *Geophys. Res. Lett.*, *32*, L20311, doi:10.1029/2005GL024296.

Hanssen, R. F. (2001), *Radar Interferometry: Data Interpretation and Error Analysis*, 1st ed., 326 pp., Springer, Netherlands.

Haran, T., J. Bohlander, T. Scambos, T. Painter, and M. Fahnestock (2005), MODIS Mosaic of Antarctica 2003–2004 (MOA2004) image map, *Tech. Rep.*, Natl. Snow and Ice Data Cent., Boulder, Colo., doi:10.7265/N5ZK5DM5.

Haran, T., J. Bohlander, T. Scambos, T. Painter, and M. Fahnestock (2014), MODIS Mosaic of Antarctica 2008–2009 (MOA2009) image map, *Tech. Rep.*, Natl. Snow and Ice Data Cent., Boulder, Colo., doi:10.7265/N5KP8037.

Helm, V., A. Humbert, and H. Miller (2014), Elevation and elevation change of Greenland and Antarctica derived from Cryosat-2, *Cryosphere*, *8*(4), 1539–1559, doi:10.5194/tc-8-1539-2014.

Hensley, S., T. Michel, M. Simard, C. Jones, R. Muellerschoen, C. Le, H. Zebker, and B. Chapman (2009a), Residual motion estimation for UAVSAR: Implications of an electronically scanned array, paper presented at 2009 IEEE Radar Conference, Pasadena, Calif., 4–8 May.

Hensley, S., H. Zebker, C. Jones, T. Michel, R. Muellerschoen, and B. Chapman (2009b), First demonstration results using the NASA/JPL UAVSAR instrument, paper presented at 2nd Annual Asia Pacific SAR Conference, Xian, China, 26–30 Oct., doi:10.1109/APSAR.2009.5374246.

Hetland, E. A., P. Musé, M. Simons, Y. N. Lin, P. S. Agram, and C. J. DiCaprio (2012), Multiscale InSAR Time Series (MInTS) analysis of surface deformation, *J. Geophys. Res.*, *117*, B02404, doi:10.1029/2011JB008731.

Hudleston, P. J. (2015), Structures and fabric in glacial ice: A review, *J. Struct. Geol.*, *81*, 1–27, doi:10.1016/j.jsg.2015.09.003.

Jezek, K. C., J. C. Curlander, F. Carsey, C. Wales, and R. G. Barry (2013), RAMP AMM-1 SAR image mosaic of Antarctica. Version 2, *Tech. Rep.*, National Snow and Ice Data Center, Boulder, Colo., doi:10.5067/8AF4ZRPULS4H.

Joughin, I. (2002), Ice-sheet velocity mapping: A combined interferometric and speckle-tracking approach, *Ann. Glaciol.*, *34*(1), 195–201, doi:10.3189/172756402781817978.

Joughin, I., D. MacAyeal, and S. Tulaczyk (2004), Basal shear stress of the Ross Ice Stream from control method inversions, *J. Geophys. Res.*, *109*, B09405, doi:10.1029/2003JB002960.

Joughin, I., R. B. Alley, and D. M. Holland (2012a), Ice-sheet response to oceanic forcing, *Science*, *338*(6111), 1172–1176, doi:10.1126/science.1226481.

Joughin, I., B. Smith, I. M. Howat, D. Floricioiu, R. B. Alley, M. Truffer, and M. Fahnestock (2012b), Seasonal to decadal scale variations in the surface velocity of Jakobshavn Isbrae, Greenland: Observation and model-based analysis, *J. Geophys. Res.*, *117*, F02030, doi:10.1029/2011JF002110.

Joughin, I., B. E. Smith, and B. Medley (2014), Marine ice sheet collapse potentially under way for the Thwaites Glacier Basin, West Antarctica, *Science*, *344*(6185), 735–738, doi:10.1126/science.1249055.

Joughin, I. R., R. Kwok, and M. A. Fahnestock (1998), Interferometric estimation of three-dimensional ice-flow using ascending and descending passes, *IEEE Trans. Geosci. Remote Sens.*, *36*(1), 25–37, doi:10.1109/36.655315.

Kamb, B. (1991), Rheological nonlinearity and flow instability in the deforming-bed mechanism of ice stream motion, *J. Geophys. Res.*, *96*(B10), 16,585–16,595, doi:10.1029/91JB00946.

King, E. C., R. C. A. Hindmarsh, and C. R. Stokes (2009), Formation of mega-scale glacial lineations observed beneath a West Antarctic ice stream, *Nat. Geosci.*, *2*, 585–588, doi:10.1038/ngeo581.
King, E. C., H. D. Pritchard, and A. M. Smith (2016), Subglacial landforms beneath Rutford Ice Stream, Antarctica: Detailed bed topography from ice-penetrating radar, *Earth Syst. Sci. Data*, *8*(1), 151–158, doi:10.5194/essd-8-151-2016.
Lohman, R., and M. Simons (2005), Some thoughts on the use of InSAR data to constrain models of surface deformation: Noise structure and data downsampling, *Geochem. Geophys. Geosyst.*, *6*, Q01007, doi:10.1029/2004GC000841.
MacAyeal, D. (1989), Large-scale ice flow over a viscous basal sediment—Theory and application to ice stream-B, Antarctica, *J. Geophys. Res.*, *94*(B4), 4071–4087.
Makinson, K., M. A. King, K. W. Nicholls, and G. Hilmar Gudmundsson (2012), Diurnal and semidiurnal tide-induced lateral movement of Ronne Ice Shelf, Antarctica, *Geophys. Res. Lett.*, *39*, L10501, doi:10.1029/2012GL051636.
Minchew, B. M. (2016), Mechanics of deformable glacier beds, PhD thesis, California Inst. of Technol., Pasadena, Calif., doi:10.7907/Z9MS3QN2.
Minchew, B. M., M. Simons, S. Hensley, H. Björnsson, and F. Pálsson (2015), Early melt-season velocity fields of Langjökull and Hofsjökull ice caps, central Iceland, *J. Glaciol.*, *61*(226), 253–266, doi:10.3189/2015JoG14J023.
Minchew, B. M., M. Simons, M. Morlighem, H. Björnsson, F. Pálsson, S. Hensley, and E. Larour (2016), Plastic bed beneath Hofsjökull Ice Cap, central Iceland, and the sensitivity of ice flow to surface meltwater flux, *J. Glaciol.*, *62*(231), 147–158, doi:10.1017/jog.2016.26.
Morlighem, M., H. Seroussi, E. Larour, and E. Rignot (2013), Inversion of basal friction in Antarctica using exact and incomplete adjoints of a higher-order model, *J. Geophys. Res. Earth Surf.*, *118*, 1746–1753, doi:10.1002/jgrf.20125.
Mouginot, J., E. Rignot, and B. Scheuchl (2014), Sustained increase in ice discharge from the Amundsen Sea Embayment, West Antarctica, from 1973 to 2013, *Geophys. Res. Lett.*, *41*, 1576–1584, doi:10.1002/2013GL059069.
Murray, T., A. M. Smith, M. A. King, and G. P. Weedon (2007), Ice flow modulated by tides at up to annual periods at Rutfurd Ice Stream, West Antarctica, *Geophys. Res. Lett.*, *34*, L18503, doi:10.1029/2007GL031207.
Nicholls, K. W., S. Osterhus, K. Makinson, T. Gammelsrod, and E. Fahrbach (2009), Ice-ocean processes over the continental shelf of the southern Weddell Sea, Antarctica: A review, *Rev. Geophys.*, *47*, RG3003, doi:10.1029/2007RG000250.
Padman, L., and H. A. Fricker (2005), Tides on the Ross Ice Shelf observed with ICESat, *Geophys. Res. Lett.*, *32*, L14503, doi:10.1029/2005GL023214.
Padman, L., H. A. Fricker, R. Coleman, S. Howard, and L. Erofeeva (2002), A new tide model for the Antarctic ice shelves and seas, *Ann. Glaciol.*, *34*(1), 247–254, doi:10.3189/172756402781817752.
Padman, L., S. Y. Erofeeva, and H. A. Fricker (2008), Improving antarctic tide models by assimilation of ICESat laser altimetry over ice shelves, *Geophys. Res. Lett.*, *35*, L22504, doi:10.1029/2008GL035592.
Paolo, F. S., H. A. Fricker, and L. Padman (2015), Volume loss from Antarctic ice shelves is accelerating, *Science*, *348*(6232), 327–331, doi:10.1126/science.aaa0940.
Perol, T., and J. R. Rice (2015), Shear heating and weakening of the margins of West Antarctic ice streams, *Geophys. Res. Lett.*, *42*, 3406–3413, doi:10.1002/2015GL063638.
Pollard, D., R. M. DeConto, and R. B. Alley (2015), Potential Antarctic Ice Sheet retreat driven by hydrofracturing and ice cliff failure, *Earth Planet. Sci. Lett.*, *412*, 112–121, doi:10.1016/j.epsl.2014.12.035.
Pritchard, H. D., R. J. Arthern, D. G. Vaughan, and L. A. Edwards (2009), Extensive dynamic thinning on the margins of the Greenland and Antarctic ice sheets, *Nature*, *461*, 971–975, doi:10.1038/nature08471.
Pritchard, H. D., S. R. M. Ligtenberg, H. A. Fricker, D. G. Vaughan, M. R. van den Broeke, and L. Padman (2012), Antarctic ice-sheet loss driven by basal melting of ice shelves, *Nature*, *484*, 502–505, doi:10.1038/nature10968.
Raymond, C. (1996), Shear margins in glaciers and ice sheets, *J. Glaciol.*, *42*(140), 90–102.
Reeh, N., E. L. Christensen, C. Mayer, and O. B. Olesen (2003), Tidal bending of glaciers: A linear viscoelastic approach, *Ann. Glaciol.*, *37*(1), 83–89, doi:10.3189/172756403781815663.
Riel, B., M. Simons, P. Agram, and Z. Zhan (2014), Detecting transient signals in geodetic time series using sparse estimation techniques, *J. Geophys. Res. Solid Earth*, *119*, 5140–5160, doi:10.1002/2014JB011077.
Rignot, E., G. Casassa, P. Gogineni, W. Krabill, A. Rivera, and R. Thomas (2004), Accelerated ice discharge from the Antarctic Peninsula following the collapse of Larsen B Ice Shelf, *Geophys. Res. Lett.*, *31*, L18401, doi:10.1029/2004GL020697.
Rignot, E., J. Mouginot, and B. Scheuchl (2011a), Ice flow of the Antarctic ice sheet, *Science*, *333*(6048), 1427–1430, doi:10.1126/science.1208336.
Rignot, E., J. Mouginot, and B. Scheuchl (2011b), Antarctic grounding line mapping from differential satellite radar interferometry, *Geophys. Res. Lett.*, *38*, L10504, doi:10.1029/2011GL047109.
Rignot, E., S. Jacobs, J. Mouginot, and B. Scheuchl (2013), Ice-shelf melting around Antarctica, *Science*, *341*(6143), 266–270, doi:10.1126/science.1235798.
Rignot, E., J. Mouginot, M. Morlighem, H. Seroussi, and B. Scheuchl (2014), Widespread, rapid grounding line retreat of Pine Island, Thwaites, Smith and Kohler glaciers, West Antarctica from 1992 to 2011, *Geophys. Res. Lett.*, *41*, 3502–3509, doi:10.1002/2014GL060140.
Rignot, E. J. (1998a), Radar interferometry detection of hinge-line migration on Rutford Ice Stream and Carlson Inlet, Antarctica, *Ann. Glaciol.*, *27*, 25–32.
Rignot, E. J. (1998b), Fast recession of a West Antarctic Glacier, *Science*, *281*(5376), 549–551, doi:10.1126/science.281.5376.549.
Rodriguez, E., and J. Martin (1992), Theory and design of interferometric synthetic aperture radars, *IEE Proc. F Radar Sign. Proces.*, *139*(2), 147–159.
Rosen, P. A., S. Hensley, I. R. Joughin, F. K. Li, S. N. Madsen, E. Rodriguez, and R. M. Goldstein (2000), Synthetic aperture radar interferometry, *Proc. IEEE*, *88*(3), 333–382, doi:10.1109/5.838084.
Rosen, P. A., S. Hensley, G. Peltzer, and M. Simons (2004), Updated repeat orbit interferometry package released, *Eos Trans. AGU*, *85*(5), 47–47, doi:10.1029/2004EO050004.
Rosen, P. A., E. Gurrola, G. F. Sacco, and H. Zebker (2012), The InSAR scientific computing environment, paper presented at 9th European Conference on Synthetic Aperture Radar, 23–26 Apr.
Rosier, S. H. R., G. H. Gudmundsson, and J. A. M. Green (2014), Insights into ice stream dynamics through modelling their response to tidal forcing, *Cryosphere*, *8*(5), 1763–1775, doi:10.5194/tc-8-1763-2014.
Rosier, S. H. R., G. H. Gudmundsson, and J. A. M. Green (2015), Temporal variations in the flow of a large Antarctic ice-stream controlled by tidally induced changes in the subglacial water system, *Cryosphere*, *9*(4), 1649–1661, doi:10.5194/tc-9-1649-2015.
Scambos, T. A., M. J. Dutkiewicz, J. C. Wilson, and R. A. Bindschadler (1992), Application of image cross-correlation to the measurement of glacier velocity using satellite image data, *Remote Sens. Environ.*, *42*(3), 177–186, doi:10.1016/0034-4257(92)90101-O.

Scambos, T. A., J. A. Bohlander, C. A. Shuman, and P. Skvarca (2004), Glacier acceleration and thinning after ice shelf collapse in the Larsen B embayment, Antarctica, *Geophys. Res. Lett.*, *31*, L18402, doi:10.1029/2004GL020670.
Scambos, T. A., T. M. Haran, M. A. Fahnestock, T. H. Painter, and J. Bohlander (2007), MODIS-based Mosaic of Antarctica (MOA) data sets: Continent-wide surface morphology and snow grain size, *Remote Sens. Environ.*, *111*(2–3), 242–257, doi:10.1016/j.rse.2006.12.020.
Scheuchl, B., J. Mouginot, and E. Rignot (2012), Ice velocity changes in the Ross and Ronne sectors observed using satellite radar data from 1997 and 2009, *Cryosphere*, *6*(5), 1019–1030, doi:10.5194/tc-6-1019-2012.
Schmeltz, M., E. Rignot, and D. R. Macayeal (2001), Ephemeral grounding as a signal of ice-shelf change, *J. Glaciol.*, *47*(156), 71–77, doi:10.3189/172756501781832502.
Schoof, C. (2007), Ice sheet grounding line dynamics: Steady states, stability, and hysteresis, *J.Geophys. Res.*, *112*, F03S28, doi:10.1029/2006JF000664.
Simons, M., and P. Rosen (2015), Interferometric synthetic aperture radar geodesy, in *Treatise on Geophysics*, 2nd ed., edited by G. Schubert, pp. 339–385, Elsvier, Amsterdam, doi:10.1016/B978-0-444-53802-4.00061-0.
Smith, A. M., and T. Murray (2009), Bedform topography and basal conditions beneath a fast-flowing West Antarctic ice stream, *Quat. Sci. Rev.*, *28*(7–8), 584–596, doi:10.1016/j.quascirev.2008.05.010.
Smith, A. M., T. Murray, K. W. Nicholls, K. Makinson, G. Aðalgeirsdóttir, A. E. Behar, and D. G. Vaughan (2007), Rapid erosion, drumlin formation, and changing hydrology beneath an Antarctic ice stream, *Geology*, *35*(2), 127–130, doi:10.1130/G23036A.1.
Smith, E. C., A. M. Smith, R. S. White, A. M. Brisbourne, and H. D. Pritchard (2015), Mapping the ice-bed interface characteristics of Rutford Ice Stream, West Antarctica, using microseismicity, *J. Geophys. Res. Earth Surf.*, *120*, 1881–1894, doi:10.1002/2015JF003587.
Suckale, J., J. D. Platt, T. Perol, and J. R. Rice (2014), Deformation-induced melting in the margins of the West Antarctic ice streams, *J. Geophys. Res. Earth Surf.*, *119*, 1004–1025, doi:10.1002/2013JF003008.
Tarantola, A. (2005), *Inverse Problem Theory and Methods for Model Parameter Estimation*, Soc. for Ind. and Appl. Math., Philadelphia, Pa.
Thomas, R. (1979), The dynamics of marine ice sheets, *J. Glaciol.*, *24*(90), 167–177.
Thomas, R., E. Rignot, P. Kanagaratham, W. Krabill, and G. Casassa (2004), Force-perturbation analysis of Pine Island Glacier, Antarctica, suggests cause for recent acceleration, *Ann. Glaciol.*, *39*(1), 133–138, doi:10.3189/172756404781814429.
Thompson, J., M. Simons, and V. C. Tsai (2014), Modeling the elastic transmission of tidal stresses to great distances inland in channelized ice streams, *Cryosphere*, *8*(6), 2007–2029, doi:10.5194/tc-8-2007-2014.
Tulaczyk, S., W. B. Kamb, and H. F. Engelhardt (2000a), Basal mechanics of Ice Stream B, West Antarctica: 1. Till mechanics, *J. Geophys. Res.*, *105*(B1), 463–481, doi:10.1029/1999JB900329.
Tulaczyk, S., W. B. Kamb, and H. F. Engelhardt (2000b), Basal mechanics of Ice Stream B, West Antarctica: 2. Undrained plastic bed model, *J. Geophys. Res.*, *105*(B1), 483–494, doi:10.1029/1999JB900328.
Ulaby, F. T., R. K. Moore, and A. K. Fung (1986), *Microwave Remote Sensing: Active and Passive*, Artech House, Dedham, Mass.
Wessel, P., W. H. F. Smith, R. Scharroo, J. F. Luis, and F. Wobbe (2013), Generic Mapping Tools: Improved version released, *Eos Trans. AGU*, *94*(45), 409–410, doi:10.1002/2013EO450001.
Zebker, H. A., and J. Villasenor (1992), Decorrelation in interferometric radar echoes, *IEEE Trans. Geosci. Remote Sens.*, *30*(5), 950–959.
Zebker, H. A., S. Hensley, P. Shanker, and C. Wortham (2010), Geodetically accurate InSAR data processor, *IIEEE Trans. Geosci. Remote Sens.*, *48*(12), 4309–4321, doi:10.1109/TGRS.2010.2051333.